Modeling of Buildings to Simulate the Effects of Vertical Components of Ground Motions

by

HENNING TYVAND

THESIS

for the degree of

MASTER OF SCIENCE

(Master i Anvendt matematikk og mekanikk)

Faculty of Mathematics and Natural Sciences
University of Oslo

29.05.2012

Det matematisk- naturvitenskapelige fakultet
Universitetet i Oslo

Acknowledgements

I owe my deepest gratitude to my external supervisor Dr. Emrah Erduran at NORSAR who gave me the opportunity to perform this research project. Throughout the past year, he has offered invaluable support and guidance which has sincerely motivated me to achieve great knowledge in earthquake analysis of structure mechanics. He has from the very begining of this research project always been available and motivated to help me out.

I would like to give a special thanks to my supervisor at the university of Oslo Dr. Harald Osnes for great support throughout this project and to complete my master's thesis. His extraordinary level of knowledge has always inspired me and I am honored to be one of his many students.

I am thankful to all members of the P3 section at NORSAR who have provided me with lots of good memories during the past year.

Finally, an honorable mention goes to my family and friends for their understanding and support throughout this project. Especially Semko Majidian, Mathias Hansen, Gjermund Kolvik and my brother Jon-Erik Tyvand .

Henning Tyvand

Oslo, Blindern.

Abstract

In general notice, the horizontal component of ground motions will normally always play the dominant role for response of buildings compared to the response from the vertical component. Therefore, the vast literature is well written for modeling of buildings to simulate the effect of horizontal components of ground motions. However, with the relatively recent recognition that the vertical component of ground motion can exceed its horizontal counterpart, there is a renewed interest in vertical ground motions and their impact on buildings.

In practical earthquake engineering, modeling of buildings to simulate effects of ground motions are based on simplified methods such as the lumped mass approach and Bernoulli beam elements. The objective in this thesis has been to maintain the simplicity in these assumptions and generalize them to determine whether a simplified model is suitable to simulate the effect of vertical motion. To evaluate the accuracy of simplified models, they are compared to an *exact* model which includes extremely refined element mesh.

The eigenvalue analysis has to a great extent been dominant for the investigation. Comparing both natural horizontal and vertical mode shapes and periods for different models, has been essential to determine which simplified model with least amount of computational effort can simulate realistic vertical motion. It is the Author's belief that studies in this thesis show that simplified models can be used to simulate vertical motion. Nevertheless, the common modeling assumption in earthquake pratice cannot be used to simulate realistic vertical motion. This applies especially to the rigid diaphragm assumption when modeling the slab.

Furthermore, response parameters from time history analysis of a suite of ground motions, shows that simplified models can simulate the effect of vertical ground motion with reliable accuracy compared to the *exact* solution.

Contents

Chapter 1

Introduction

Throughout this introductory chapter, the motivation, specification, scope and outline follows.

1.1 Motivation

The common practice in earthquake analysis of buildings is to ignore the vertical component of ground motions and analyze the structure under horizontal components of the ground motion. In general earthquake analysis, buildings are mostly modeled by using Bernoulli beam elements to model beams and columns without physically modeling the slab system. The effects of slabs are simulated implementing rigid-diaphragm constraint for the nodes that are at the same floor level. The mass of each floor is assumed to be lumped at the center of mass of the floor. Although this approach works perfectly fine for analysis of buildings under horizontal ground motions only, it has been observed that lumped mass models can lead to unrealistic mode shapes and deformation patterns when the vertical component of the ground motion is included in the analysis. With the increasing interest in vertical ground motions, modeling of buildings to simulate the effects of vertical motions remains to be a major challenge for the earthquake engineering community.

From a historical point of view, horizontal component amplitudes of ground motions normally plays the dominant role compared to the vertical counterpart. However, acceleration records from the January 17, 1994, Northridge earthquake in the United States, the January 17, 1995, Hyogoken earthquake in Japan and the February 22, 2011, Christchurch earthquake in New Zealand, among others, showed that the magnitudes of the vertical component can be as large, or exceed, the horizontal component. hence, research on this topic is limited. Iyengar and Shinozuka [2] used a cantilever beam to investigate the effect of the vertical component of earthquakes. Ariaratnam and Leung [1] analyzed a 2D story frame building and concluded that the vertical acceleration causes the reduction of the column stiffness and increases the lateral displacement. Sadeghvaziri and Foutch [4] pointed out that vertical vibration leads to the instability of columns. The effects of the vertical component of earthquake motion were studied by Gupta and Hutchinson [3] using a simple lumped-mass model of a single story building resting on a rigid foundation. All these aforementioned studies was conducted on 1D or 2D vases with limited degrees of freedom. However, in a study conducted by Ju *et al.* [5] a systematic study of 3D analyses was analyzed to investigate the extreme column axial forces and beam moments between vertical earthquake and dead

loads. Nevertheless, simplified models with least amount of computational effort to simulate the effects of vertical motions appears to be absent in the literature.

With the relatively recent recognition that the vertical component of ground motions can be as high, or even exceed the horizontal counterpart, efforts towards modeling buildings to simulate the effects of vertical ground motions has been done. However, taken into account that normal modeling procedure in earthquake engineering is based on simplified assumptions, the intention is to maintain the simplicity in these assumptions and generalize them to model buildings to simulate realistic vertical motion. To server the *exact* solution, highly improved element meshes in finite element softwares are used. Much effort has been done to create highly refined models so that the accuracy of simplified models can be reliable when they are compared to the *exact* solution. The main intention of this thesis is to determine which of the simplified modes, with least amount of computational effort, can simulate realistic vertical motion.

It is worthwhile to note that some modern finite element softwares allows structures components to be modeled with perfection using a very fine mesh of elements using consistent mass approach. However, the computational efforts for these advanced finite element softwares are much higher than general engineering software. On the other hand, different alternative modeling approaches in a general engineering software (OpenSEES) are developed in order to assess the efficiency of these models in capturing the vertical and horizontal vibration modes. The most efficient modeling approach, i.e. the approach that requires least effort while maintaining sufficient accuracy, is identified.

1.2 Specifications

In this thesis, the following steps will be accomplished

1. A set of model buildings with different structural systems will be analyzed in ANSYS using a finite element modeling (FEM) approach. The structural systems will be modeled in their entirety including all structural members and slab systems. The masses will be modeled as continuous masses throughout the structural members and slabs. Eigenvalue-value and elastic response history analysis under a suite of ground motions will be conducted to evaluate the vibration modes and characteristics of the model buildings. As such, the full FEM models will provide a realistic representation of the model buildings and will serve as "benchmark" to evaluate the efficiency and accuracy of simplified models that will be developed in the further stages.

2. Model buildings will be re-modeled using the lumped-mass assumption in OpenSEES. Eigen-value and elastic response history analysis conducted in step 1 will be repeated using the lumped-mass model and the results will be compared to investigate and document the shortcomings of the lumped-mass model.

3. Efforts will be put towards eliminating the shortcomings of the lumped-mass models that have been identified in step 2. The accuracy of the simplified approaches in capturing the vertical vibration modes and deformation patterns of the buildings will be investigated for:

   (a) using multiple elastic beam elements to simulate the effects of slabs

   (b) explicit modelling of slabs using plate elements

   (c) explicit modelling of slabs using shell elements

4. For all approaches in step 3, several meshing options from coarse to very fine will be analyzed to determine the optimum mesh configuration. The results of eigen-value analysis and elastic response history analysis obtained from these improved models will be compared to the benchmark results for evaluation. The most efficient model that can simulate the behavior of buildings under vertical ground motions will be identified.

1.3 Scope

Different modeling approaches, based on the lumped mass approach, of buildings are created to simulate the effects of vertical component of ground motions. Coarse to fine lumped mass models, as well as the slab, classifies the accuracy for each model compared to the exact solution. Both 2D and 3D multiple-degree-of-freedom buildings are included in the analysis, where eigenvalue analyses to a great extent determines the reliability of each model to capture realistic vertical motion when they are compared to the *exact* solution. Numerical time history analyses are performed, but limited to the 2D range only. In this case, both horizontal and vertical component of recorded ground motions are included in the analysis. All analyses performed are modeled and calculated in finite element software.

Although earthquake analysis for buildings normally render the inelastic range, this study involves only the elastic range and eigenvalue analysis and time history analysis are used to solve equation of motion. Shear deformation and second order effects are neglected. Symmetrical buildings are used.

1.4 Outline

To serve the specifications, the thesis is divided into two parts.

Part I provides some of the necessary theoretical background needed to understand the complexity of the specifications in this thesis. Throughout part I, some fundamental theory and applications for earthquake engineering are explained within the elastic range. With advanced knowledge in theory and applications to earthquake engineering, part I may not be necessary to go through for fully understand the later on results. However, taken into account that the terminology that is used in this part carries on throughout the entire report, it is recommended to briefly overview the main equations and algorithms.

Chapters 2 in Part I introduce a general introduction to the equation of motion subjected to ground motion. Time history analysis and eigenvalue analysis are the methods used in this thesis to solve equation of motion, and Chapter 3 provides theory of these methods. Based on that finite element software's are used extensively to solve the methods in Chapter 3, Chapter 4 defines how to determine the parameters in equation of motion in a finite element range. The last chapter 5, in Part I, is general seismology.

Part II introduces modeling procedures, assumptions and restrictions of the thesis. Chapter 7 presents the 2D model and Chapter 8 the 3D model. In both Chapters 7 and 8, modeling procedure, analysis, results and discussion are provided. Conclusion and recommendation for further studies is the last chapter.

Part I

THEORETICAL BACKGROUND: DYNAMICS OF STRUCTURES SUBJECTED TO EARTHQUAKE ACTION

Chapter 2

Equation Of Motion: Earthquake Excitation

This chapter introduces equation of motion due to ground motion for single-degree-of-freedom (SDOF) systems and then due to multiple-degree-of-freedom (MDOF) systems. Equation of motion mathematically describes the behavior of structures under dynamic loading and is developed by Newtons second law and D'Alembert's principle of motion [6]. In general form, equation of motion can be defined as

$$m\ddot{u}(t) + c\dot{u}(t) + ku(t) = p(t) \tag{2.0.1}$$

where : m is mass, c is damping, k is stiffness and the dynamic response of the structure to the dynamic loading p is defined by the acceleration $\ddot{u}(t)$ is acceleration, velocity $\dot{u}$, and displacements u.

2.1 Single-degree-of-freedom systems

Fig. 2.1.1 shows the ground displacement $u_g(t)$ and the relative displacement between the mass and ground $u_r(t)$. This gives total (or absolute) displacement of the mass $u_{tot}(t)$.

For each instant of time, the relationship between $u_g(t)$ and $u_r(t)$ can be expressed

$$u_{tot}(t) = u_r(t) + u_g(t) \tag{2.1.1}$$

If the system in figure 2.1.1 consider only one DOF, say lateral displacement of u_{tot}, and the mass is concentrated at one location with the rest of the frame massless, it can be idealized as an one-story system (although the static analysis problem has to be formulated with three DOFs). The mass is in this case lumped.

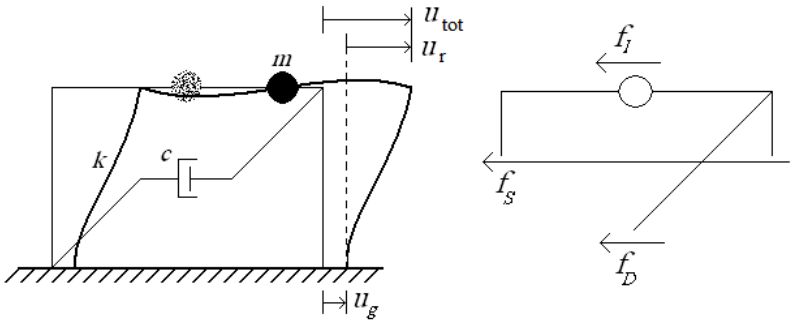

Figure 2.1.1: Singel degree of freedom system; Displacement conditions due to ground displacement. And internal forces of the system.

The equation of motion for the idealized one-story system of fig. 2.1.1 can be developed by using the concept of dynamic equilibrium. Dynamic equilibrium is satisfied when

$$f_I + f_D + f_S = 0 \tag{2.1.2}$$

where $f_I = m\ddot{u}_{tot}(t)$ is the inertia force, $f_D = c\dot{u}_r(t)$ is the damping force and $f_S = ku_r(t)$ is the lateral stiffness force, respectively. Inertia force $f_I = m\ddot{u}_{tot}(t)$ is based on the total displacement $u_{tot}(t)$, because that is the total displacement of the mass. Meanwhile, elastic force $f_D = ku_r(t)$ and damping force $f_S = c\dot{u}_r(t)$ only depends on relative motions $u_r(t)$ and $\dot{u}_r(t)$, respectively.

From these relationships, Eq.(2.1.2) and (2.1.1) can be rewritten as

$$m\left(\ddot{u}_r(t) + \ddot{u}_g(t)\right) + c\dot{u}_r(t) + ku_r(t) = 0$$

which is equal to

$$m\ddot{u}_r(t) + c\dot{u}_r(t) + ku_r(t) = -m\ddot{u}_g(t) \tag{2.1.3}$$

Eq.(2.1.3) is called equation motion subjected to a ground acceleration $\ddot{u}_g(t)$, or more general equation of ground motion.

The relative displacement $u_r(t)$ of the structure due to the ground acceleration $\ddot{u}_g(t)$ is identical to the total displacement position of the structure if the structure is standing on a stationary base exposed by an external force $-m\ddot{u}_g(t)$. Therefore, the right side of Eq.(2.1.3) can be replaced by what is called the effective earthquake force $p_{eff}(t) = -m\ddot{u}_g(t)$ showed in Fig 2.1.2. $p_{eff}(t) = -m\ddot{u}_g(t)$ is the dynamic loading in Eq. (2.0.1) and is related to ground motion.

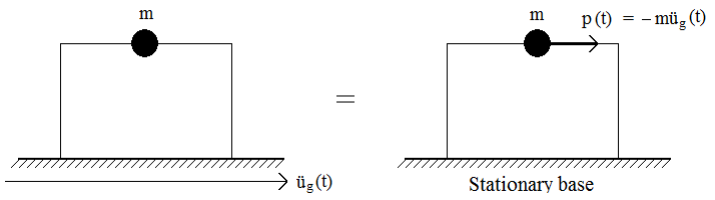

Figure 2.1.2: Ground motion $\ddot{u}_g$ represented as a force connected to the mass location of the SDOF system.

The effective earthquake force is proportional to the total mass of the structure, which means that the mass (m) and effective earthquake force $p_{eff}(t)$ increase equally.

2.2 Multiple-degree-of-freedom systems

The same principles as for SDOF systems are also valid for MDOF systems. In SDOF systems, the mass (m), stiffness (k) and damping (c) are regained a single scalar quantity, while they are represented as matrices in MDOF systems. Matrices are designated with bold capital letters inside brackets [], and vectors with bold capital letters inside loop parentheses {}.

The total displacement from Eq. (2.1.1) is for a MDOF system combined in vector form such as

$$\{\mathbf{U}\}_{tot}(t) = \{\mathbf{U}\}_r(t) + u_g(t)\{\mathbf{i}\} \tag{2.2.1}$$

where $\mathbf{i}$ is the *influence vector* representing the displacements of the masses of a unit ground displacement.

Using the same concept of dynamic equilibrium as introduced for SDOF systems, dynamic equilibrium is satisfied for MDOF systems when

$$\{\mathbf{F}\}_I + \{\mathbf{F}\}_D + \{\mathbf{F}\}_S = \mathbf{0} \tag{2.2.2}$$

and now, $[\mathbf{F}]_I = [\mathbf{M}]\{\ddot{\mathbf{U}}\}_{tot}(t)$ is the inertia force matrix, $[\mathbf{F}]_D = [\mathbf{C}]\{\dot{\mathbf{U}}\}_r(t)$ is the damping force matrix and $[\mathbf{F}]_S = [\mathbf{K}]\{\mathbf{U}\}_r(t)$ is the stiffness force matrix, respectively.

Combining Eq. (2.2.1) and (2.2.2) leads to the equation of ground motion of MDOF system such as

$$[\mathbf{M}]\{\ddot{\mathbf{U}}\}_{\mathbf{r}}(t) + [\mathbf{C}]\{\dot{\mathbf{U}}\}_r(t) + [\mathbf{K}]\{\mathbf{U}\}_r(t) = -[\mathbf{M}]\{\mathbf{i}\}\ddot{u}_g(t) \tag{2.2.3}$$

The effective earthquake force $\{\mathbf{p}\}_{eff}(t) = -[\mathbf{M}]\{\mathbf{i}\}\ddot{u}_g(t)$ are related with the same conditions as for SDOF systems showed in Fig. 2.1.2 but with several mass positions.

Later in this thesis, solutions of equation of motion are solved with both horizontal and vertical component of the ground motion. Equation of motion subjected to two components of the ground can be express

$$[\mathbf{M}]\{\ddot{\mathbf{U}}\}_{\mathbf{r}}(t) + [\mathbf{C}]\{\dot{\mathbf{U}}\}_r(t) + [\mathbf{K}]\{\mathbf{U}\}_r(t) = -[\mathbf{M}]\{\{\mathbf{i_x}\}\ddot{u}_{gx} + \{\mathbf{i_y}\}\ddot{u}_{gy}\}(t) \tag{2.2.4}$$

where x and y are horizontal and vertical components, respectively.

Chapter 3

Analysis Methods

This chapter provides two analysis methods to solve different applications of equation of motion [2.0.1] for multiple-degree-of-freedom systems, such as eigenvalue analysis and time history analysis. Mathematical expressions and explanations of these two methods are provided. In part II, both of these methods are used to analyze a suite of different models.

3.1 Eigenvalue Analysis

The first analysis method is the eigenvalue analysis, and it is limited to free vibration only. Free vibration of systems is the motion of a structure without any dynamic excitation. Solutions of eigenvalue analysis are natural mode shapes and frequencies of a structure. Free vibrations of systems play a central role in dynamic and earthquake analysis of linear systems when modal analyses are general application to solve equation of motion. However, modal analyses are not provided or used in this thesis.

3.1.1 Natural vibration frequencies and mode shapes

This subsection develops the notion of natural frequencies and natural modes of MDOF systems. A systematic mathematical build-up of how to assume free vibration of equation of motion and the solve natural properties such as mode shapes and vibrations are provided.

Natural vibrations frequencies and mode shapes of an undamped system can be developed by reduce equation of motion (2.2.3) to

$$[\mathbf{M}]\{\ddot{\mathbf{U}}\}(t) + [\mathbf{K}]\{\mathbf{U}\}(t) = \{\mathbf{0}\} \tag{3.1.1}$$

Solution of time variation of displacements $\{\mathbf{U}\}(t)$ gives a system that oscillates with constant peaks. However, an eigenvalue analysis is not a problem solved in the time domain, but in the frequency domain. Therefore, the natural mode shape$\{\phi\}_n$ does not vary with time. The free vibration of an undamped system can then be described by

$$\{\mathbf{U}\}(t) = q_n(t)\{\phi\} \tag{3.1.2}$$

where the time variation of the displacements $q_n(t)$ is described by the harmonic function

$$q_n(t) = A_n cos(\omega_n t) + B_n sin(\omega_n t) \tag{3.1.3}$$

where A_n and B_n are constants determined by the initial conditions that initiate the motion.

Combining Eq. (3.1.2) and (3.1.3) gives

$$\{\mathbf{U}\}(t) = \{\phi\}_n \left(A_n cos\left(\omega_n t\right) + B_n sin\left(\omega_n t\right)\right) \tag{3.1.4}$$

where ω_n and ϕ_n are unknown.

Furthermore, substituting Eq.(3.1.4) in Eq.(3.1.1) and then twice derive this with respect of time gives

$$\left[-\omega_n^2[\mathbf{M}]\{\phi\}_n + [\mathbf{K}]\{\phi\}_n\right] q_n(t) = \{\mathbf{0}\} \tag{3.1.5}$$

This equation (3.1.5) has two solutions in order to be satisfied. One solution is the trivial solution, $q_n(t) = 0$, which means that the displacements $\{\mathbf{U}\}(t) = 0$ from Eq. (3.1.2). The other solution requires that the natural frequencies and mode shapes satisfies

$$\begin{aligned} -\omega_n^2[\mathbf{M}]\{\phi\}_n + [\mathbf{K}]\{\phi\}_n &= \\ \left[[\mathbf{K}] - \omega_n^2[\mathbf{M}]\right]\{\phi\}_n &= [\mathbf{0}] \end{aligned} \tag{3.1.6}$$

which is called the *matrix eigenvalue problem.* This equation as also two solution in order to be satisfied, and $\{\phi\}_n = 0$ is the trivial. Natural frequencies can then be determined by

$$det\left[[\mathbf{K}] - \omega_n^2[\mathbf{M}]\right] = \{\mathbf{0}\} \tag{3.1.7}$$

Solutions of ω_n^2 can then mode shapes $\{\phi\}_n$ in Eq. (3.1.6).

In summary, a MDOF vibration system has N natural vibration frequencies ω_{jn} and modes $\{\phi\}_{jn}$, where $j = 1, 2, ..., N$. They are arranged in sequence from smallest to largest $\omega_{1n} < \omega_{2n} < ... < \omega_{Nn}$; Corresponding natural frequencies ω_{jn} and natural modes shapes $\{\phi\}_{jn}$.

Normalization of modes

The eigenvalue problem, Eq. (3.1.6), only determines natural modes within a multiplicative factor. if the vector $\{\phi\}_n$ is a natural mode, any vector proportional to $\{\phi\}_n$ is the same natural mode because it also satisfies Eq. (3.1.6). Scale factors can be applied to natural modes to standardize their elements associated with various DOF. This process is called *normalization*. Normally this is on the top of a multistory building.

Normalization are much necessary to perform in this thesis when mode shapes from different models are compared to each other.

Solution methods to solve the eigenvalue problem

Finding the vibration properties requires solution of the *matrix eigenvalue problem* of Eq. (3.1.6). The eigenvalues are the roots of the characteristic equation (3.1.7);

$$p(\lambda) = det\left[\mathbf{K} - \lambda\mathbf{M}\right] = 0 \tag{3.1.8}$$

where $p(\lambda)$ is a polynomial of order N in being the number of DOFs of the system. However, using the determinant to solve the matrix eigenvalue problem is not a practical method because evaluation of the N coefficients of the polynomial requires much computational effort, and the roots of $p(\lambda)$ are sensitive to numerical round-off errors. Thus, for large matrices, reliable and efficient methods to solve the eigenvalue problem is needed. Hand calculations cannot be performed to solve this, and the computer as a calculation tool is necessary.

All solution methods for eigenvalue problems must be solved iterative, naturally because solving the eigenvalue problem is equivalent to finding the roots of the polynomial $p(\lambda)$ and no explicit formulas are available for these roots when N is larger than 4 [17].

In this thesis, finite element software's that solve Eq. (3.1.8) uses subspace iteration or the Lanczos method. However, these methods are not explained here, but can be found in [25,16].

3.2 Time history analysis

Time history analysis methods directly solve equation of motion in time domain. With implicit or explicit integrations methods, both SDOF and MDOF systems can be solved within the elastic or inelastic range. In earthquake analysis, an implicit algorithm to solve equation of motion is favored [6]. Based on that, this section contains an implicit direct integration method emphasizing the Newmark's method for MDOF systems. However, only a short introduction of the method is presented. This method is used later when time history analyses are performed.

3.2.1 Implicit direct integration method

Direct integration of Eq. (2.2.3) refers to step-by-step calculation of response history in time. Direct integration methods evaluate response separately at each instant of time $\triangle t$ (e.g. recorded ground motion). With an implicit integration method, the time step is $n+1$. Equation of motion (2.2.4) subjected by two components of the ground motion can then be expressed

$$\left[\mathbf{M}\right]\left\{\ddot{\mathbf{U}}\right\}_{n+1} + \left[\mathbf{C}\right]\left\{\dot{\mathbf{U}}\right\}_{n+1} + \left[\mathbf{K}\right]\left\{\mathbf{U}\right\}_{n+1} = -\left[\mathbf{M}\right]\left\{\{\mathbf{i_x}\}\ddot{u}_{gx+1} + \{\mathbf{i_y}\}\ddot{u}_{gy+1}\right\} \tag{3.2.1}$$

Newmark's method

Newmark's method contains numerical factors γ and β that control characteristics of the algorithm such as accuracy and numerical stability. for MDOF systems, Newmark relations of the $\{\mathbf{U}\}$ vector of d.o.f are

$$\left\{\dot{\mathbf{U}}\right\}_{n+1} = \left\{\dot{\mathbf{U}}\right\}_{n} + \Delta t\left[\gamma\left\{\ddot{\mathbf{U}}\right\}_{n+1} + (1-\gamma)\left\{\ddot{\mathbf{U}}\right\}_{n}\right] \tag{3.2.2}$$

$$\{\mathbf{U}\}_{n+1} = \{\mathbf{U}\}_n + \Delta t \left\{\dot{\mathbf{U}}\right\}_n + \frac{1}{2}\Delta t^2 \left[2\beta \left\{\ddot{\mathbf{U}}\right\}_{n+1} + (1-2\beta)\left\{\ddot{\mathbf{U}}\right\}_n\right] \tag{3.2.3}$$

Solving Eq. (3.2.3) for $\left\{\ddot{\mathbf{U}}\right\}_{n+1}$ and substituting this expression into Eq. (3.2.2) gives

$$\left\{\ddot{\mathbf{U}}\right\}_{n+1} = \frac{1}{\beta\Delta t^2}\left(\{\mathbf{U}\}_{n+1} - \{\mathbf{U}\}_n - \Delta t\left\{\dot{\mathbf{U}}\right\}_n\right) - \left(\frac{1}{2\beta} - 1\right)\left\{\ddot{\mathbf{U}}\right\}_n \tag{3.2.4}$$

$$\left\{\dot{\mathbf{U}}\right\}_{n+1} = \frac{\gamma}{\beta\Delta t^2}\left(\{\mathbf{U}\}_{n+1} - \{\mathbf{U}\}_n\right) - \left(\frac{\gamma}{\beta} - 1\right)\left\{\ddot{\mathbf{U}}\right\}_n - \Delta t\left(\frac{\gamma}{2\beta} - 1\right)\left\{\ddot{\mathbf{U}}\right\}_n \tag{3.2.5}$$

Eqs. (3.2.3), (3.2.5) and (3.2.4) can now be substituted into the equation of motion (3.2.1) and then solve for $\left\{\ddot{\mathbf{U}}\right\}_{n+1}$.

To begin calculations, $\left\{\ddot{\mathbf{U}}\right\}_0$ needs to be calculated. A step by step procedure of this is summarized in [10].

Accuracy and stability

To provide accuracy, $\left\{\ddot{\mathbf{U}}\right\}_0$ cannot be set as $\left\{\ddot{\mathbf{U}}\right\}_0 = \{\mathbf{0}\}$ unless the mass matrix is diagonal such as an lumped mass approach. Forcing $\left\{\ddot{\mathbf{U}}\right\}_0$ to zero, may reduce the accuracy from second-order to first-order [12]. Evaluating $\left\{\ddot{\mathbf{U}}\right\}_0$ requires that $[\mathbf{M}]$ is assembled and reduced for equation-solving.

Furthermore, Newmark method have *unconditional stability* when

$$2\beta \geq \gamma \geq \frac{1}{2} \tag{3.2.6}$$

and *conditional stability* when

$$\gamma \geq \frac{1}{2} \qquad \beta < \frac{1}{2}\gamma \qquad \nabla t = \frac{\Omega_{crit}}{\omega_{max}}$$

where

$$\Omega_{crit} = \frac{\zeta\left(\gamma - \frac{1}{2}\right) + \sqrt{\frac{\gamma}{2} - \beta + \xi^2\left(\gamma - \frac{1}{2}\right)^2}}{\frac{\gamma}{2} - \beta}$$

in which ζ is the damping ratio.

However, *conditionally stable* implicit method are rarely used in practice, because of the severe constraint placed on Δt and the substantial cost per time step of an implicit method in 2D and 3D problems. *Unconditional stability* is a computational cheaper and even very large values of Δt do not make calculations "blow up"[7].

Chapter 4

Methods to Define Stiffness, Mass and Damping

This chapter provides theories of how to define stiffness [**K**], mass [**M**] and damping [**C**] in equation of motion when modeling MDOF systems. The purpose of this chapter is to understand the effect of using different methods to define stiffness and mass when solving applications of equation of motion.

The principle of minimum potential energy (PMPE) can provide the relations of stiffness and mass. PMPE has been used because finite element softwares used in this thesis are based on this principle. Applications on how to define stiffness is not provided. However, the mass matrix methods are divided into two subsections. The first provides the consistent mass matrix from PMPE, and the other is the lumped mass approach. Taken into account that determine natural mode shapes and vibration periods plays a dominant role in this thesis, evaluating stiffness and mass are considered necessary and reasonable to include.

4.1 Stiffness matrix

There is a vast literature describing theories and methods to understand stiffness of structures, such as; Material properties, boundary conditions and methods to describe geometric structural properties. The stiffness contribution from material properties and boundary conditions appears as a result of defined limits of a structure. However, geometrical properties depends of a method's ability to involve actual physical phenomena, e.g., bending, shear deformation, torsional deformations and/or second order effects (often called P-delta effects). However, only shear deformation effects are explained within detail in this section.

Furthermore, this section provides theories of how to evaluate the stiffness of beams and plates in structures when the principle of minimum potential energy is used. However, a profound implementation in finite element methods is explained in [7]. Nevertheless, further presentations are based on the presumptation that the reader is familiar with the finite element method for analysis of static structural problems.

Elastic Stiffness matrix: Stiffness matrix from PMPE can be written as

$$[\mathbf{K}^e] = \int [\mathbf{B}]^T [\mathbf{E}] [\mathbf{B}] \, dV \tag{4.1.1}$$

where $[\mathbf{K}^e]$ is the local stiffness matrix (local matrices are assigned with raised e), $[\mathbf{B}] = \frac{d^2}{dx^2} \{\mathbf{N}\}$, where $\{\mathbf{N}\}$ are the shape functions of beams or plates and $[\mathbf{E}]$ is constitutive matrix.

4.1.1 Shear and bending deformation effects

This subsection introduces both beams and plate theories including or neglecting first order shear deformation effects. However, a deep understating of the theories are not provided.

Beam theories

In Finite Element Analyses, shape functions can be described by evaluating interpolations of an element. Interpolate is to device a continuous function that satisfies prescribe conditions at nodes. For 2D beams with two degrees of freedom in each end, rotation θ and translation V showed in Fig. 4.1.2, the shape functions can be expressed by the shape function vector $\{\mathbf{N}\}^T = \{N_1, N_2, N_3, N_4\}$. Where N_i represents each interpolation showed in Fig.4.1.1.

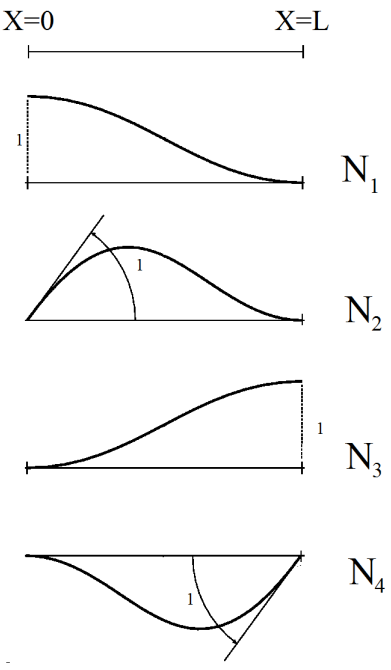

Figure 4.1.1: Shape functions N_i for the 2D beam element. Slopes at $x = 0$ and $x = L$.

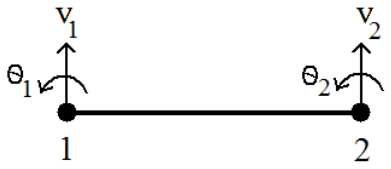

Figure 4.1.2: Positive definitions of the shape functions in Fig. x. θ is rotational degree of freedom and V is translation.

Euler Bernoulli beam theory

Euler Bernoulli beam theory invokes zero shear stress assumptions which results in zero transverse shear deflection. The displacement field implies that straight lines normal to the mid plane before deformation remain straight and normal to the mid plane after deformation, showed in Fig 4.1.3. Although the restrictions of neglecting shear deformation is an approximation of the reality, the error is considered small when beams are reasonably slender [7]. This theory is often referred as classic beam theory.

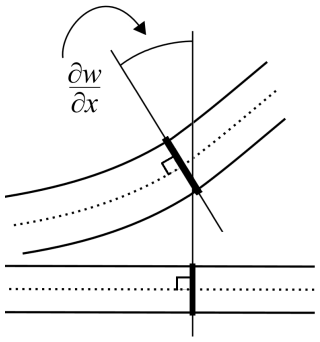

Figure 4.1.3: Euler-Bernoulli beam: Undeformed state and deformed state retained Naviers hypotese.

From this relation, the shape functions for 2D beams can be expressed

$$\{\mathbf{N}\} = \begin{Bmatrix} 1 - 3\left(\frac{x}{L}\right)^2 + 2\left(\frac{x}{L}\right)^3 \\ L\left(\frac{x}{L} - 2\left(\frac{x}{L}\right)^2 + \left(\frac{x}{L}\right)^3\right) \\ 3\left(\frac{x}{L}\right)^2 - 2\left(\frac{x}{L}\right)^3 \\ L\left(-\left(\frac{x}{L}\right)^2 + \left(\frac{x}{L}\right)^3\right) \end{Bmatrix} \tag{4.1.2}$$

In terms of accuracy, these shape functions describes bending exact [7].

The local stiffness matrix for Bernoulli beams $[\mathbf{K}^e]_{Bernoulli}$ can then be expressed by Eq. (4.1.1)

$$[\mathbf{K}^e]_{Bernoulli} = \int_0^L [\mathbf{B}]^T [\mathbf{E}] [\mathbf{B}] \, dx = \frac{EI}{L^3} \begin{bmatrix} 12 & 6L & -12 & 6L \\ 6L & 4L^2 & -6L & 2L^2 \\ -12 & -6L & 12 & -6L \\ 6L & 2L^2 & -6L & 4L^2 \end{bmatrix} \tag{4.1.3}$$

Timoshenko beam theory

Timoshenko beam theory introduced first order shear deformation for beam theory. This theory is also called *first order shear deformation beam theory*. In Timoshenko beam theory, the normlaity of Euler-Bernoulli beam theory is relaxed and a constant state of the transverse shear strain with respect to the thickness coordinate is included. Fig. 4.1.4 shows deformed and undeformed state of the Timoshenko beam, where the normal in underformed shape rotates by Φ. The error of constant shear stress distribution through the beam depth in Timoshenko beam theory, requires the shear correction Φ to compensate [9]. For Bernoulli, the normal is always the angle $\frac{dw}{dx}$.

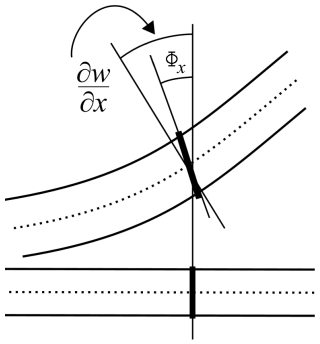

Figure 4.1.4: Timoshenko beam theory. The normal rotates by Φ.

From the relation of how first order shear deformation is included in Timoshenko beam theory, the shape functions for 2D beams can be expressed

$$[\mathbf{N}] = \left\{ \begin{array}{c} \frac{1}{1+\Phi}\left[1-3\left(\frac{x}{L}\right)^2+2\left(\frac{x}{L}\right)^3+\left(1-\frac{x}{L}\right)\Phi\right] \\ \frac{1}{1+\Phi}\left[\frac{x}{L}-2\left(\frac{x}{L}\right)^2+\left(\frac{x}{L}\right)^3+\frac{1}{2}\left(\frac{x}{L}-\left(\frac{x}{L}\right)^2\right)\Phi\right] \\ \frac{1}{1+\Phi}\left[3\left(\frac{x}{L}\right)^2-2\left(\frac{x}{L}\right)^3+\frac{x}{L}\Phi\right] \\ \frac{1}{1+\Phi}\left[-\left(\frac{x}{L}\right)^2+\left(\frac{x}{L}\right)^3-\frac{1}{2}\left(\frac{x}{L}-\left(\frac{x}{L}\right)^2\right)\Phi\right] \end{array} \right\} \tag{4.1.4}$$

This will from Eq. (4.1.1) give the local stiffness matrix for Timoshenko beam theory

$$\begin{aligned} [\mathbf{K}^e]_{Timoshenko} &= \int_0^L [\mathbf{B}]^T [\mathbf{E}] [\mathbf{B}] \, dx \\ &= \frac{EI}{(1+\Phi) L^3} \begin{bmatrix} 12 & 6L & -12 & 6L \\ 6L & (4+\Phi) L^2 & -6L & (2-\Phi) L^2 \\ -12 & -6L & 12 & -6L \\ 6L & (2-\Phi) L^2 & -6L & (4+\Phi) L^2 \end{bmatrix} \end{aligned} \tag{4.1.5}$$

The term Φ gives the relative importance of the shear deformations to the bending deformations, showed in Fig. 4.1.4.

$$\Phi = \frac{12EI}{G\left(\frac{A}{\alpha}\right) L^2}$$

$\frac{A}{\alpha}$ is the effective shear area for transverse shear deformation. Determining the shear correction factor can be done with different methods, however, in engineering practices, Timoshenko provided general expressions assumed good enough [9]. For solid rectangular cross section, the shear correction factor can be assumed $\alpha = \frac{5}{6}$.

When elements becomes more and more slender, Φ approaches zero and the shear deformation contribution progressively decreases. Neglecting all shear deformation can be done by specify $\Phi = 0$.

Plate and shell theories

Plates and shell can be described with and without shear deformation effects as well. Kirchhoff and Mindlin-Reissner plate theories are mentioned in this section, although it is not provided a mathematical understanding which was provided for beams. For the interested reader, this can be found in [11].

Kirchhoff plate theory

The Kirchhoff plate theory is an extension of Euler–Bernoulli beam theory restricted to thin plates $\frac{t}{L} < \frac{1}{10}$. Where t denotes the plate thickness and L denotes the length of the plate. Kirchhoff's plate theory do not include shear deformation effects. Thin plates must satisfy C^0- continuity, which implies the shape functions to be continuity after first derivative. The classic thin plate theory is based on *Kirchhoff hypothesis*:

- Straight lines perpendicular to the mid-surface before deformation remain straight after deformation
- The transverse normal do not experience elongation
- The transverse normals rotate such that they remain perpendicular to the mid-surface after deformation.

The consequence of the Kirchhoff hypothesis is that the transverse strains are zero, and consequently, the transverse stresses do not enter the theory.

Mindlin- and Reissner plate theory

Mindlin- and Reissner plate theory include first order shear deformation recommended for thick plates $\frac{1}{3} > \frac{t}{L} > \frac{1}{10}$.

Mindlin plate theory invoke plane stress, while Reissner includes the possibility that the plate thickness may change during deformation – which is not a possibility in Mindlin theory. Mindlin and Reissner is in general called Mindlin-Reissner plate theory, despite their profound differences in assumptions and formulations [8]. Misunderstanding of the differences in Mindlin- and Reissner plate theory causes that, in practical engineering, both Mindlin- or Reissner plate theory results in the same shear deflection contribution. A deep understanding of both theories can be found in [8].

4.1.2 Stiffness approach of slender buildings in general engineering pratice

In general engineering, buildings is normally modeled using one element for each structural member. This benefits Euler Bernoulli beam theory when this practically makes it impossible for Timoshenko beam theory to satisfy the requirement of thick beams to obtain shear deformation [11]. Neglecting shear deformation in general structural engineering is an assumption made out of that building components normally contain slender structural members and shear deformation effects are small compared to bending. However, including shear deformation effects when defining the stiffness matrix indicates that bigger deformations are possible which results in slower periods.

4.1.3 Second order effects

The axial force in a structure contributes on the stiffness. Tensile force increases the stiffness so that the structure can resist displacements perpendicular of the axial force better. On the other hand, compressive forces reduces the stiffness and displacements perpendicular of the axial force increases.

Generally, vertical components in buildings exposure compressive forces because of the buildings weight and the gravity force. Compressive forces in the vertical components increases the displacements perpendicular of the axial force, and the base moment increases. This effects can be called *geometrical effects* or *P-delta effects*, expressed as F_G. F_G is approximately proportional to the displacement and can be written as

$$F_G(t) = [\mathbf{K}_g] \{\mathbf{U}\}_r (t)$$

where $[\mathbf{K}_g]$ is geometrical stiffness [24,20].

This extra moment force can be included in the equation of motion such as

$$[\mathbf{M}]\{\ddot{\mathbf{U}}\}_{\mathbf{r}}(t) + [\mathbf{C}] \{\dot{\mathbf{U}}\}_r(t) + [\mathbf{K}] \{\mathbf{U}\}_r(t) - [\mathbf{K}_g] \{\mathbf{U}\}_r (t) = - [\mathbf{M}]\{\mathbf{i}\}\ddot{u}_g(t)$$

Reduction of the stiffness matrix directly indicates that bigger deformations are possible, which results in slower natural periods.

4.2 Mass matrix methods

For a real building, the mass is distributed over each and single physical element of the building. This way to model the mass is not profitable to be practiced for solving the equation of motion because that provides the mass matrix, theoretically, to be infinite big. However, continuous mass distribution can be discrete represented as a mass matrix idealized as consistent or lumped. In general earthquake engineering, the lumped mass approach is generally used based on that only the horizontal component of ground motions are considered in the analysis.

This section provides the consistent and lumped mass approach.

4.2.1 Consistent mass matrix

Mentioned in the stiffness matrix section, shear deformation effects improved the deformation pattern. As shown, the shape functions for beam elements are different for Bernoulli and Timoshenko. That is the case for the consistent mass matrix as well, because the matrix develops from the shape functions for an element with the relationship

$$[\mathbf{M}^e] = \int_0^L \{\mathbf{N}\}^T \{\mathbf{N}\} \rho A \, dx \tag{4.2.1}$$

where $\{\mathbf{N}\}$ is the shape function vector, ρ is the density and A is the area of the cross section.

This provides a full mass matrix largely parallels that of the stiffness matrix. Consistent mass matrix for individual element are formed in local coordinates, transformed to global, and merged into the global consistent mass matrix following exactly the same techniques used for solving the stiffness matrix, $[\mathbf{K}]$. For Bernoulli beam theory, the consistent mass matrix for each element is created from the shape functions of Eq. (4.1.2) to be

$$[\mathbf{M}^e]_{Bernoulli} = \int_0^L \{\mathbf{N}\}^T \{\mathbf{N}\} \rho A \, dx = \frac{m}{420} \begin{bmatrix} 156 & 22L & 54 & -13L \\ 22L & 4L^2 & 13L & -3L^2 \\ 54 & 13L & 156 & -22L \\ -13L & -3L^2 & -22L & 4L^2 \end{bmatrix} \tag{4.2.2}$$

and for Timoshenko beam theory involving shear deflection from Eq. (4.1.4) to be

$$\begin{aligned} [\mathbf{M}^e]_{Timoshenko} &= \int_0^L \{\mathbf{N}\}^T \{\mathbf{N}\} \rho A \, dx \\ &= \frac{m}{840} \begin{bmatrix} 312+588\Phi+280\Phi & \left(44+77\Phi+35\Phi^2\right) L \\ \left(44+77\Phi+35\Phi^2\right) L & L\left(8+14\Phi+7\Phi^2\right) L^2 \\ 108+252\Phi+175\Phi^2 & \left(26+63\Phi+35\Phi^2\right) L \\ -\left(26+63\Phi+35\Phi^2\right) L & -\left(6+14\Phi+7\Phi^2\right) L^2 \end{bmatrix} \\ &\quad \begin{bmatrix} 108+252\Phi+175\Phi^2 & -\left(26+63\Phi+35\Phi^2\right) L \\ \left(26+63\Phi+35\Phi^2\right) L & -\left(6+14\Phi+7\Phi^2\right) L^2 \\ 312+588\Phi+280\Phi^2 & -\left(44+77\Phi+35\Phi^2\right) L \\ -\left(44+77\Phi+35\Phi^2\right) L & \left(8+14\Phi+7\Phi^2\right) L^2 \end{bmatrix}_{4x4} \end{aligned} \tag{4.2.3}$$

This indicates that the consistent mass matrix is different for Bernoulli beam theory and Timoshenko beam theory. However, if $\Phi = 0$ there are no differences..

Plate elements regarding Kirchhoff and Mindling theory can be found in [22,21].

4.2.2 Lumped mass matrix

The lumped mass matrix approach results in diagonal matrix where mass is assigned to nodes and is determined for the portion of the weight that can reasonably be assigned to the node, showed in Fig. 4.2.1.

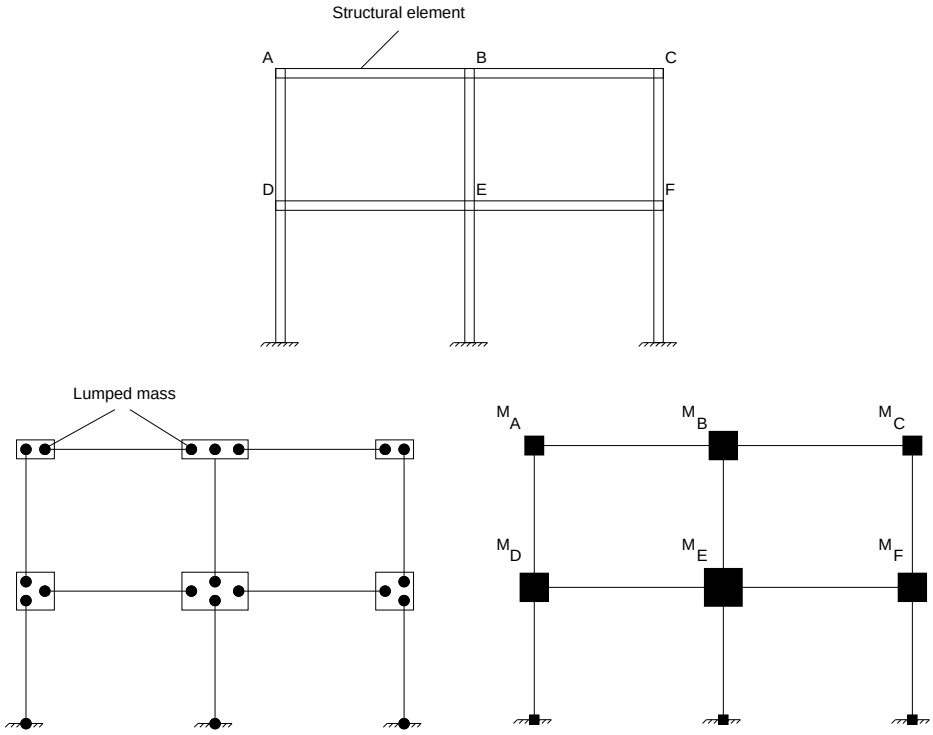

Figure 4.2.1: Lumped mass approach.

This implies that each structural element share a point mass at its nodes. A notable difference with the stiffness matrix is the possibility of using diagonal mass matrix based on direct lumping. In case of a beam element with constant cross section, half of the mass is lumped in each node. If these masses are considered to contribute to translational motion only, the mass matrix on element level would appear as

$$[\mathbf{M}^e] = \begin{bmatrix} 1 & & & \\ & 0 & & \\ & & 1 & \\ & & & 0 \end{bmatrix} \tag{4.2.4}$$

Terms to take into account the effect of rotational inertia are usually placed in the two diagonal coefficients of Eq. (4.2.4) which now contain zeros.

Notice that regardless of what Bernoulli beam theory or Timoshenko beam theory is considered, the lumped mass approach remains the same. This is the same for plates as well.

4.2.3 Mass approach of buildings in general engineering practice

In a general building, the majority of the building's mass is distributed over the slab system and then only a very small proportion is left in the columns. Because of that, the mass from the columns is normally included in the lumped mass approach, showed in Fig 4.2.1. This modeling procedure is common practice in structural engineering and earthquake engineering when modeling buildings.

For horizontal motion without distributing the mass in the columns, the lumped mass as-

sumptions increases accuracy for buildings with the relationship; Total slab mass >> total column mass, in which this implies that the mass of the columns barley constitute any mass.

4.3 Damping matrix

Unlike the stiffness and mass matrices, damping matrix cannot be computed using matrial and physical properties. There are many significant part of the energy dissipation that could not explicitly been taken into account such as; friction of steel connections, opening and closing of microcracks in concrete, fire-proofing friction between structure and non-structural components. Therefore, damping of MDOF systems is generally determined by numerical values for the damping ratios assigned to individual nodes, bases on experimental data for similar structures. Different damping ratios can be determine from modal damping ratios which account for energy-dissipating of mechanism. Damping ratios of different materials can be estimated from earthquakes, where the buildings components do not enter the inelastic range [6]. Different materials and conditions of structures is listed up in Table 4.3.1. Normally assumption of damping ratio for concrete buildings is 5%.

Table 4.3.1: Recommended damping values, [13]

Stress Level	Type and Condition of Structure	Damping Ratio (%)
Working stress, no more than about $\frac{1}{2}$ yield point	Welded steel, prestressed concrete, well-reinforced concrete (only slight cracking)	2–3
	Reinforced concrete with considerable cracking	3–5
	Bolted and/or riveted steel, wood structures with nailed or bolted joints	5–7
At or just below yield point	Welded steel, prestressed concrete (without complete loss in prestress)	5–7
	Prestressed concrete with no prestress left	7–10
	Reinforced concrete	7–10
	Bolted and/or riveted steel, wood structures with bolted joints	10–15
	Wood structures with nailed joints	15–20

4.3.1 Rayleigh Damping

This subsection introduces how to calculate the damping matrix using the Rayleigh damping theory. An eigenvalue analysis is required to determine solutions of frequencies which is needed in Rayleigh damping theory.

Rayleigh damping have the relation

$$[\mathbf{C}] = a_0 [\mathbf{M}] + a_1 [\mathbf{K}] \tag{4.3.1}$$

where the constants a_0 and a_1 have the units of sec^{-1} and sec, respectively.

The damping ratio for the nth mode (from the eigenvalue analysis) is

$$\zeta_n = \frac{a_0}{2}\frac{1}{\omega_n} + \frac{a_1}{2}\omega_n \tag{4.3.2}$$

From specified damping ratios Constants ζ_i and ζ_j, a_0 and a_1 can be determined for the ith and $j$the mode, respectively. Eq. (4.3.2) can be expressed in a matrix form such as

$$\frac{1}{2}\begin{bmatrix} \frac{1}{\omega_i} & \omega_i \\ \frac{1}{\omega_j} & \omega_j \end{bmatrix}\begin{Bmatrix} a_0 \\ a_1 \end{Bmatrix} = \begin{Bmatrix} \zeta_i \\ \zeta_j \end{Bmatrix} \tag{4.3.3}$$

Based on experimental data, it is reasonable to assume that both modes have the same damping ratio. Eq. (4.3.3) can then be rewritten as

$$a_0 = \zeta\frac{2\omega_i\omega_j}{\omega_i + \omega_j}, \qquad a_1 = \zeta\frac{2}{\omega_i + \omega_j} \tag{4.3.4}$$

Applying this procedure to a practical problem, the ith and jth mode should be those modes which contributes significantly to the response, because only these modes will have exactly 5% damping. Fig. 4.3.1 shows the relationship of the damping ratio ζ and natural frequencies ω_i and ω_j.

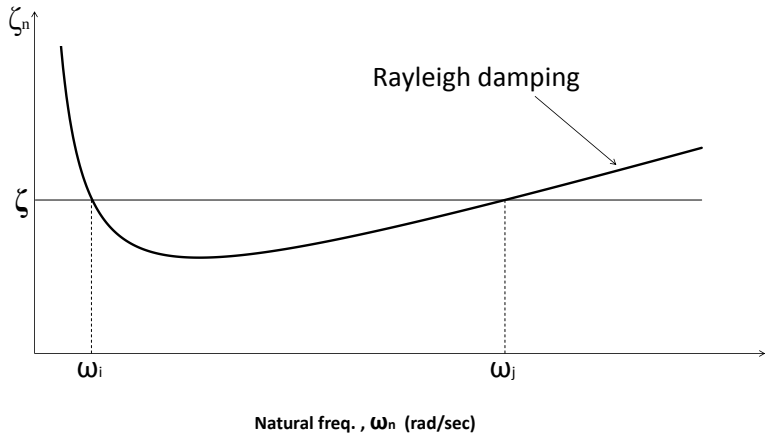

Figure 4.3.1: Variation of modal damping ratios with natural frequency for Rayleigh damping.

Fig. 4.3.1 shows that the damping for the modes in between ω_i and ω_j gives somewhat less damping, while those after ω_j gives more. The damping ratio for modes after ω_j increases monotonically and corresponding modal response essentially eliminates because of their high damping.

Chapter 5

Seismology

Seismology covers a vast field, and only a short introduction within a few theories has been given in this chapter. How earthquakes occur, elastic waves that can create dangerous earthquakes and how to record ground motions in both horizontal and vertical direction are explained.

5.1 Introduction

Seismology is the scientific study of earthquakes and the propagation of elastic waves through or around the earth. In general, people relate earthquakes as collisions between tectonic plates on the Earth's surface. India, Italy and Japan are examples of this, and earthquakes often appears in these countries. Fig 5.1.1 shows epic center of all earthquakes with an amplitude over 3.5 or more in the period 1963-1998.

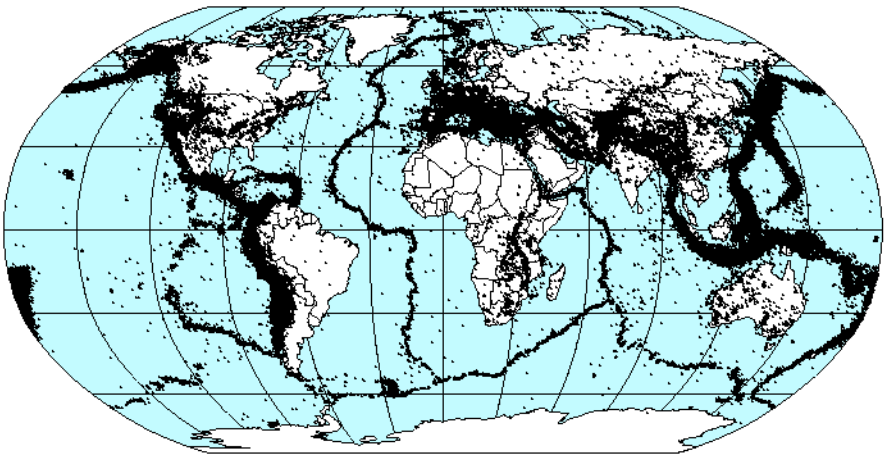

Figure 5.1.1: Overview of the epic center of all earthquakes with an amplitude of 3.5 or more in the period 1963-1998. The picture is taken from [19]

An earthquake occurs when rocks being deformed suddenly break along a fault. The two blocks of rock on both sides of the fault slip suddenly, setting off the ground vibration. This

slippage occurs most commonly at plate boundaries, regions of the Earth's crust or upper mantle where most of the ongoing deformation take place. The fault can

5.2 Body waves

Earthquake shaking and damage is the result of basic types of elastic waves. Two of them propagate within a body of rock. The faster of these body waves is called the primary or P wave and the slower ones is called the secondary or S wave, showed in Fig. 5.2.1.

P wave's motion is as it spreads out, it alternately compresses anddilates the rock. As a S wave propagates, it shears the rock sideways at right angles to the direction of travel. The actual speed of P and S seismic waves depends on the density and elastic properties of the rocks and soil through which they pass. In most earthquakes, the P waves comes first, then some seconds later, the S waves arrive and the ground surface shakes both vertically and horizontally. This is the wave motion that is so damaging to buildings.

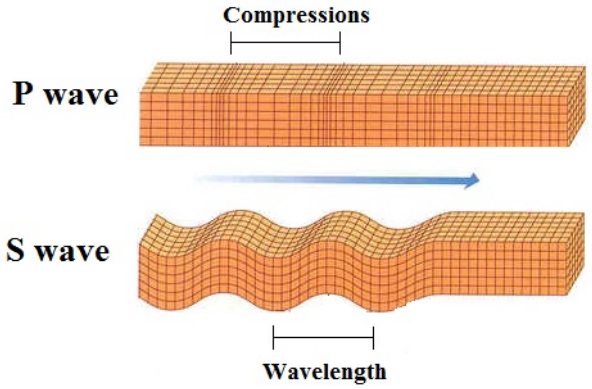

Figure 5.2.1: Visually graphic of how the P and the S wave shakes through the body. Picture from[27].

5.3 Seismometer

Seismometers are instruments that measure motions of the ground, and they are extremely sensitive to seismic waves generated by e.g. earthquakes. The seismometer makes use of the principle of inertia. If a heavy mass is only loosely coupled to the ground, as in Fig. 5.3.1, the motion of the Earth caused by a seismic wave is only partly transferred to the mass. While the ground vibrates, the inertia of the heavy mass assures that it does not move as much, if at all. The seismometer amplifies and records the relative motion between the mass and the ground, such as u_r in Fig. .

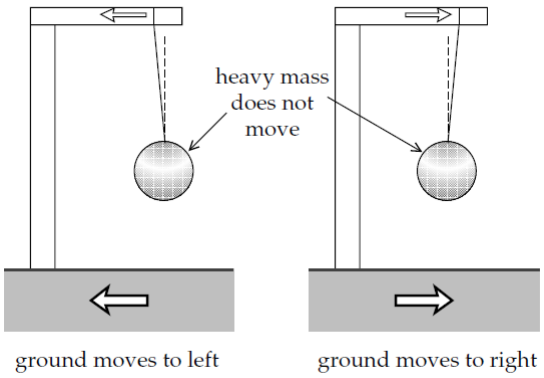

Figure 5.3.1: The principle of the seismometer. Suspended heavy mass remains stationary when the ground and suspension move to left and right. Picture from [15].

Fig. 5.3.2a and 5.3.2b shows schematically design of seismometers which can capture horizontal and vertical motion based on the principle of inertia. For the vertical-motion seismometer, a large mass is mounted on the horizontal bar hinged at a pivot so that it can move only in the vertical direction. A loose coupling between the mass and the housing is assured when a bar is held in the horizontal position by a weak spring. The theory remains the same for horizontal-motion seismometer, where the inertial mass is mounted on a horizontal bar but it is hinged vertically so the mass only can swing in the horizontal plane.

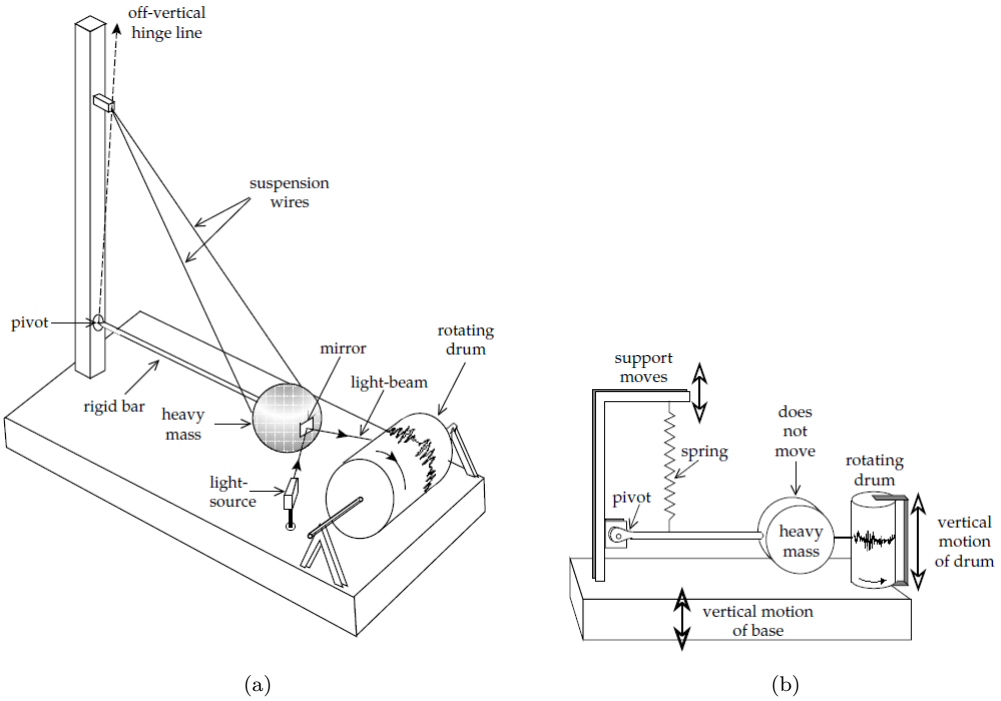

Figure 5.3.2: Schematic design illustrating the mechanical pendulum type of vertical- and horizontal-seismometer: (a) Horizontal (b) Vertical Pictures from [15].

Another instrument to record motion is the electromagnetic instruments which respond to

the velocity of ground motions[15]. Some modern electromagnetic instruments can record three orthogonal components of the motion simultaneously.

Mentioned in the motivation of this thesis, it is the general notice that the horizontal component of ground motions normally plays the dominant role. However, relatively recently recorded ground motions shows that the vertical component can exceed its counterpart. Fig. 5.3.3a and b shows how the vertical component recorded from the PRPC station from the Christchurch earthquake 2011 clearly exceeded the horizontal counterpart.

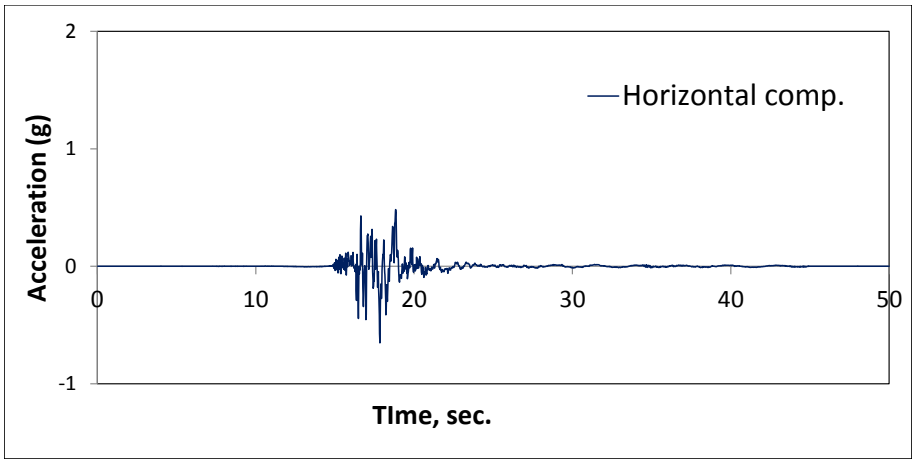

(a)

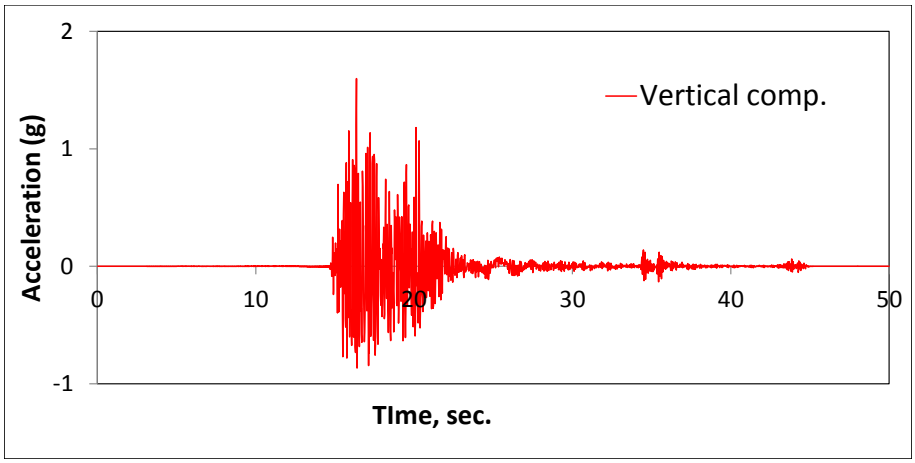

(b)

Figure 5.3.3: Horizontal and vertical ground acceleration from PRPC station of the Christchurch earthquake February 2011. (a) Horizontal component, W. PGA=0.67g (b) Vertical component, UP. PGA=1.63g.

Part II

MODELING OF BUILDINGS TO SIMULATE THE EFFECTS OF VERTICAL COMPONENTS OF GROUND MOTIONS

Chapter 6

Modeling Assumptions

This chapter introduces a short presentation of the finite element softwares and the reason why they are used in this thesis. Furthermore, assumptions, restrictions and how the modeling procedure has been done are explained.

6.1 Finite element softwares: OpenSEES and ANSYS

OpenSEES and ANSYS are the two finite element software used in this thesis. However, ANSYS is only used when modeling in 3D.

The main purpose of using OpenSEES and ANSYS, is that OpenSEES is a general engineering software using the lumped mass approach while ANSYS uses the consistent mass approach. Moreover, ANSYS is a complex finite element software and require much more computational effort than OpenSEES, which is not favored in general engineering practice.

Simplified models in OpenSEES contains classic beam elements (Bernoulli) and shell elements (Kirchhoff), while ANSYS offers more advanced elements including e.g. transverse shear deformation effects (Timoshenko and Mindlin). However, the intention in this thesis is to created simplified models using the lumped mass method and compare these models to very fine element mesh using the consistent mass approach.

Shell elements in OpenSEES uses the bilinear isoparametric formulation[23, 7] with 6 DOF in each node. Beam elements are model as elastic classic Bernoulli beams.
Models in ANSYS uses shell93 and beam4/beam189.

6.2 Assumptions and restrictions

Eigen-value analysis is to a great extent been used in this thesis to identify natural mode shapes and periods. It is assumed that determine natural mode shapes and periods from eigen-value analysis classifies the accuracy of different simplified lumped mass models when they are compared to an *exact* solution. Furthermore, it is then assumed that if a simplified lumped mass model gives very similar natural mode shapes and vibration periods compared to the exact solution, this simplified model is a reliable model to simulate vertical motions.

This assumption is based on the common modal analysis to solve equation of motion under ground motions[6]. Nevertheless, modal analysis is beyond the scope of this thesis. Instead, time history analysis is used to solve equation of ground motion.

The *exact* solution when modeling in 2D is restricted to the lumped mass approach and it is assumed that a very fine element mesh with lumped masses serves as the *Benchmark model* to simulate vertical motion.

In 3D modeling, the slab is modeled with shell elements. Shell elements are provided instead of solid elements because of a license restriction of 64 000 DOF in ANSYS. However, it is further assumed that a model with shell elements reaches out as a reliable model to simulate vertical motion because a very fine element mesh is used.

Slender component are utilized when modeling buildings in this thesis. Therefore, it is assumed that the contribution from shear deformations are very small. Based on that distributing the mass in columns are normally not modeled in engineering practice, columns are modeled without mass and one element per structural member is used.

For simplified models in 3D, only shell elements are used to model the slab.

6.3 Modeling procedures

In general earthquake engineering, modeling the slabs remains to be a challenge when the vertical component of ground motion is taken into account. Determing realistic vertical mode shapes and frequencies requires the slab to be included in the modeling procedure in 3D and several beam elements in 2D. This section start up with explaining the general lumped mass method to model buildings in earthquake engineering pratice. Thereafter, the modeling procedures of how lumped mass models are created in this thesis are explained.

6.3.1 General practice in earthquake engineering to model buildings

In earthquake engineering practice, the vertical component of ground motion is normally ignored. This implies that only the horizontal component of ground motion is taken into account when modeling buildings under earthquakes. Based on that, the lumped mass approach is normally used and Fig. 6.3.1 shows where the masses generally are placed in earthquake engineering practice.

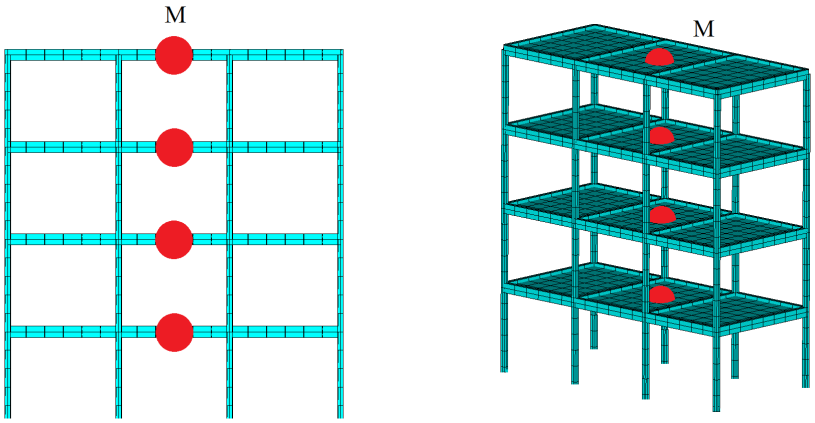

(a) 2D. (b) 3D.

Figure 6.3.1: General lumped mass configuration for earthquake modeling in 2D and 3D. Total mass for each story is lumped in the mass center.

Furthermore, the common approach in 3D is to assume the slab to be rigid in its plane, showed in Fig 6.3.2. A rigid diaphragm method can be used to achieve these preconditions, including nodes in a plane to connect to a master node. Introducing this assumption implies that both (x and y) horizontal DOFs of all the nodes at a floor level are related to the three rigid-body DOFs of the floor diaphragm in its own plane. these DOFs are defined as translation and rotation about the rigid-diaphragm axis. The mass needs only to be defined in these DOFs and no where else. This theory implies that the slab is not needed to be modeled with any elements, and therefore, it is a less computationally complex modeling procedure. In general, it is common to place the master node in the mass center and the lumped mass connected to the master node.

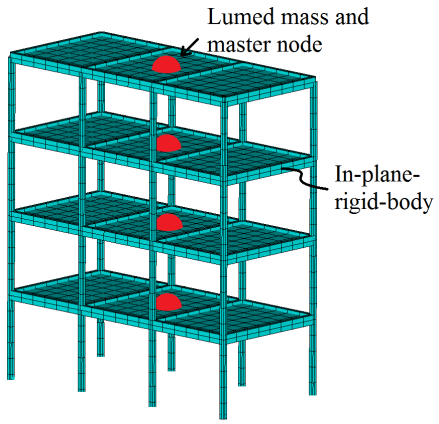

Figure 6.3.2: In-plane rigid diaphragm, lumped mass approach and master node in the middle of the geometrical center.

6.3.2 Lumped mass approach to model buildings to include vertical motion

The whole intention of using a lumped mass approach to model buildins to include vertical motion is desired because this is the common modeling approach in earthquake engineering practice. A lumped mass approach is also favored when finite element softwares in general engineering only offer this approach.

Lumping the mass is only been done over the beam and shell elements, which implies that columns is model without mass. Fig. 6.3.3 shows two lumped mass models where the lumped masses are distributed. Fig 6.3.3a shows how the mass can be lumped on top of the columns, and Fig 6.3.3b shows how the mass can be lumped on top of the columns and in the middle of each beam. Similar methodology is used in this thesis to descretesize different lumped mass approaches in both 2D and 3D problems. Coarse to very fine lumped mass models are explicitly created.

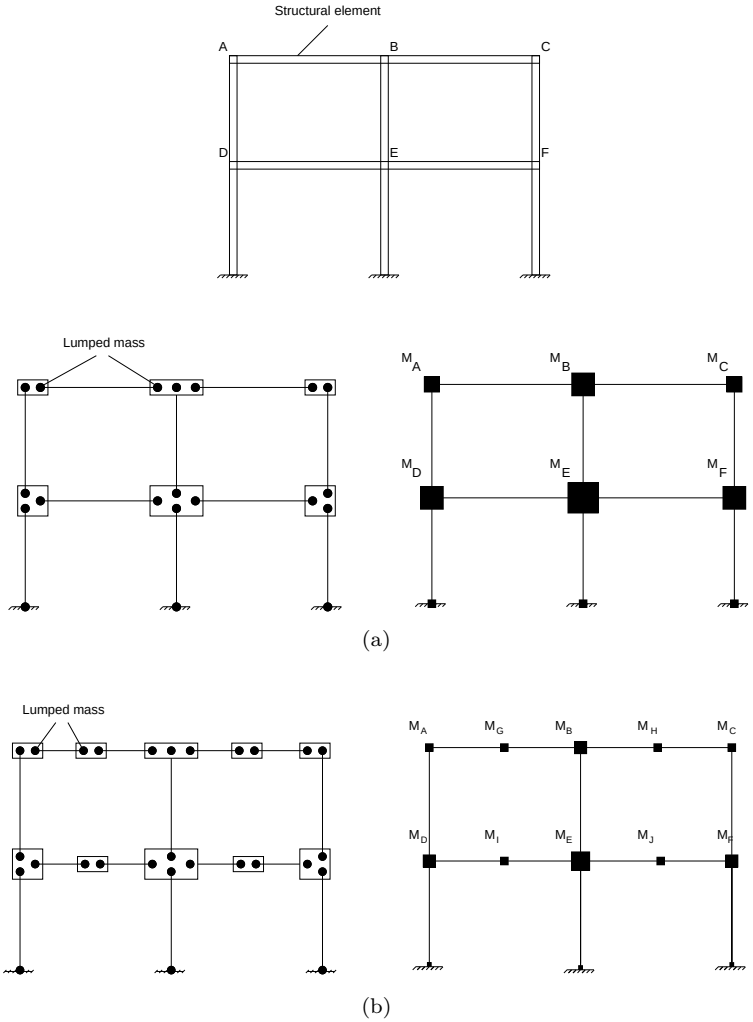

Figure 6.3.3: Lumped mass models. (a) Lumped mass on top of the columns (b) Lumped mass on top of columns and in the middle of the beam.

Chapter 7

2D Modeling, Analyses, Results and Discussion

7.1 Introduction of the building

Figure 7.1.1 represents a five story building modeled in 2D. The building is assumed to be reinforced concrete. A preliminary design to determine column and beam sites were conducted. All necessary information of the building is given in the Table 7.1.1.

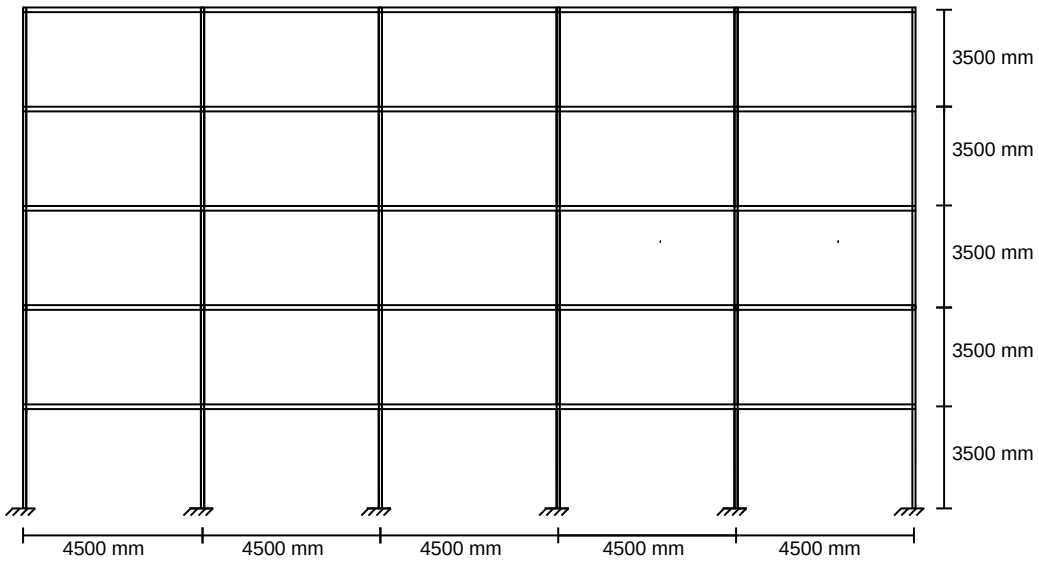

Figure 7.1.1: 2D elevation view of the five story building. All structural members are modeled as elastic.

Table 7.1.1: Structural properties for the five story building

Properties	Initials	Values
Cross section beams	$H_b \cdot B_b$	$600\,mm \cdot 300\,mm$
Cross section Columns	$H_c \cdot B_c$	$450\,mm \cdot 450\,mm$
Young-module	E	25000
Poisson's ratio	ν	0.3
Mass at each floor	m	85000 kg
Total mass	M_{tot}	425000 kg

This building is modeled in OpenSEES with coarse to very fine lumped mass models. However, ANSYS is not been used to model this building and a consistent mass approach is therefore not included to serve the *exact* solution. This implies that the *exact* solution of this building is created in OpenSEES using a lumped mass approach. However, it is assumed that a fine mesh of lumped masses serves as a reliable *exact* solution to simulate the effects of vertical components of ground motions.

Furthermore, columns are modeled with one Bernoulli beam element per structural member, and the mass from columns is neglected.

7.1.1 The benchmark model

The *Benchmark model*, showed in Fig. 7.1.2, is created in OpenSEES with 81 lumped masses over each floor. As mentioned, this very fine mesh of lumped masses are assumed to simulate the effects of vertical ground motions with good accuracy because of the very fine lumped mass distribution. m in the figure implies the total amount of mass in each floor.

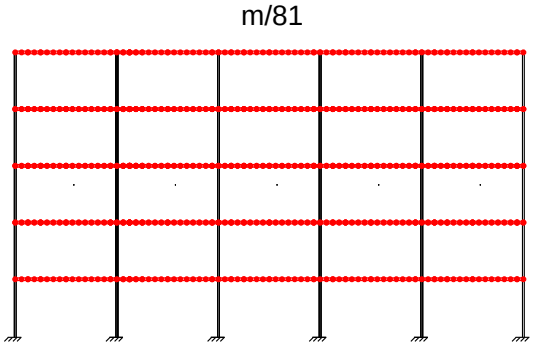

Figure 7.1.2: The *benchmark* of the 2D building. Each red dot implies a lumped mass, and there are 81 lumped masses over each floor.

7.1.2 Simplified lumped mass models

The intention is now to create simplified lumped mass models and compare these to the *Benchmark model*. Simplified lumped mass models are defined in Fig.7.1.3 and includes coarse to very fine models. Fig.7.1.3a is the common model in earthquake engineering today. Fig . 7.1.3b to 7.1.3d shows better and better distributed lumped mass models, were the last one is the most refined simplified lumped mass model.

For all subfigures in Fig. 7.1.3, m implies the total amount of mass in each floor and the relationship $\frac{m}{x}$ is the quantity of each lumped mass.

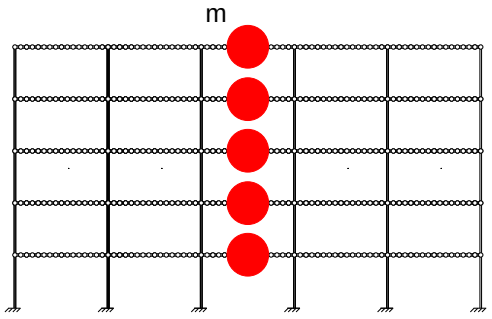

(a) *Mass model 1.*

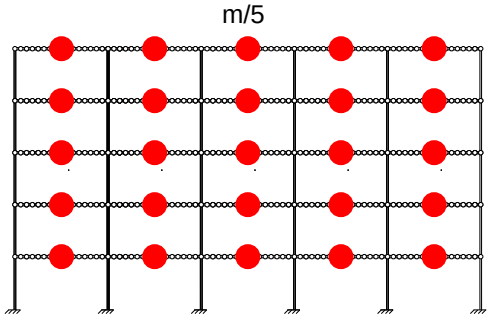

(b) *Mass model 2.*

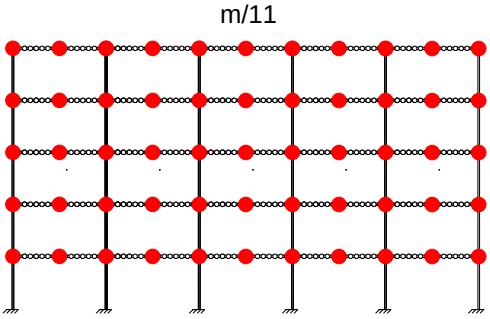

(c) *Mass model 3.*

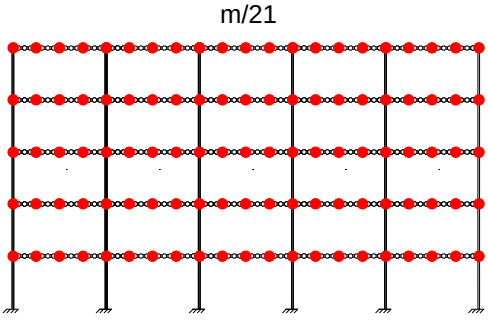

(d) *Mass model 4.*

Figure 7.1.3: Simplified lumped Mass models for the five story building. Each red point implies a lumped mass.

7.2 Discussion of results

Both Eigenvalue analysis and time history analysis of all models of the five story building are performed. The eigenvalue results and discussion are provided in the first subsection. Results and discussion from time history analysis are provided in the last subsection, but an introduction of how the time history analyses are performed and which ground motions used are first explained.

7.2.1 Eigenvalue analyses 2D

The first four modes in each direction is obtained by eigenvalue analyses in OpenSEES. Mode shapes from the *Benchmark model* and simplified models are plotted on top of each other to identify differences. The mode shapes are normalized with the quantity 1.0 at the top of the roof. Natural horizontal mode shapes and vibration periods are presented and discussed first, then comes the vertical.

Horizontal modes:

Compared to the *Benchmark model,* the horizontal mode shapes, showed in Fig 7.2.1 and 7.2.2, shows that there are very small or no differences regardless of which *Mass model* that are used. However, the horizontal periods from Table 7.2.1 implies that there are some differences in natural horizontal periods, and that they decreases with higher modes. On the other hand, the mode shapes shows that there are very small differences between models compared to the *Benchmark model* for the first two modes and that the errors increases for higher modes.

Zero or small errors for the horizontal modes implies that distribute the lumped mass mesh over beams constitute no differences. Based on these results, it is adequately to assume that *mass approach 1* is the model with less computational effort to simulates horizontal motions with reliable accuracy.

Table 7.2.1: Horizontal natural periods.

	Natural periods, T_n (sec.)			
	Mode 1	Mode 2	Mode 3	Mode 4
Mass model 1	0.728	0.241	0.145	0.108
Mass model 2	0.727	0.238	0.140	0.101
Mass model 3	0.692	0.227	0.133	0.095
Mass model 4	0.723	0.237	0.139	0.099
Benchmark model	0.710	0.232	0.136	0.098

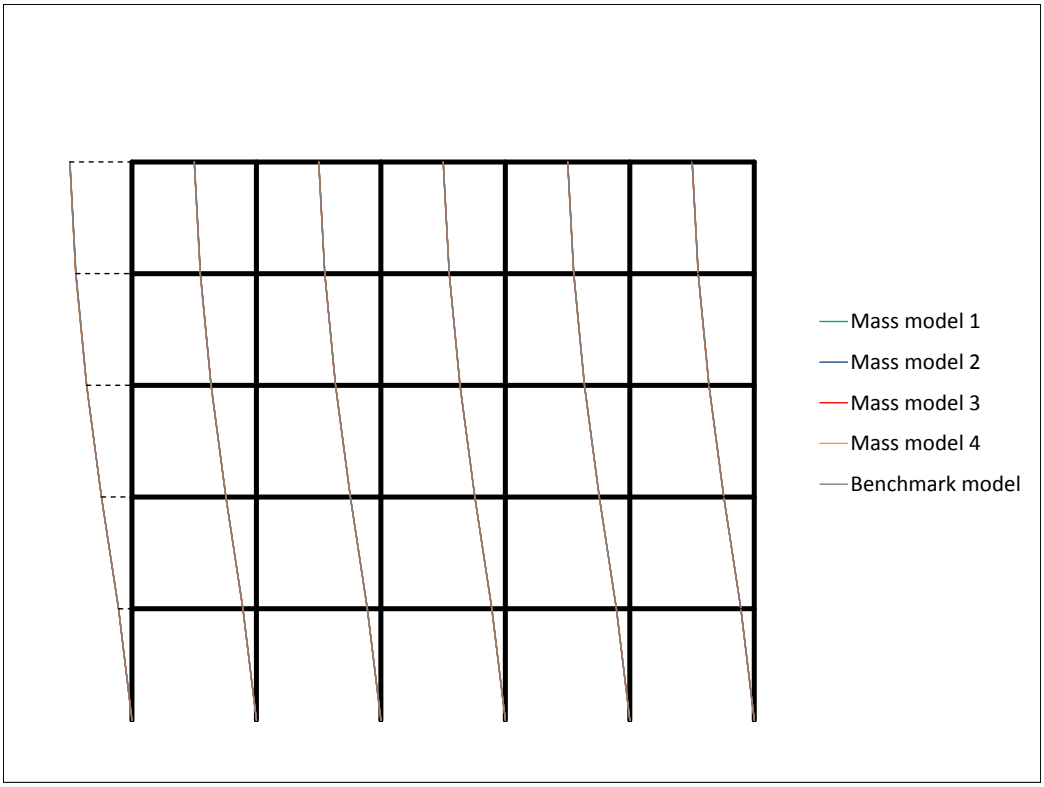

(a)

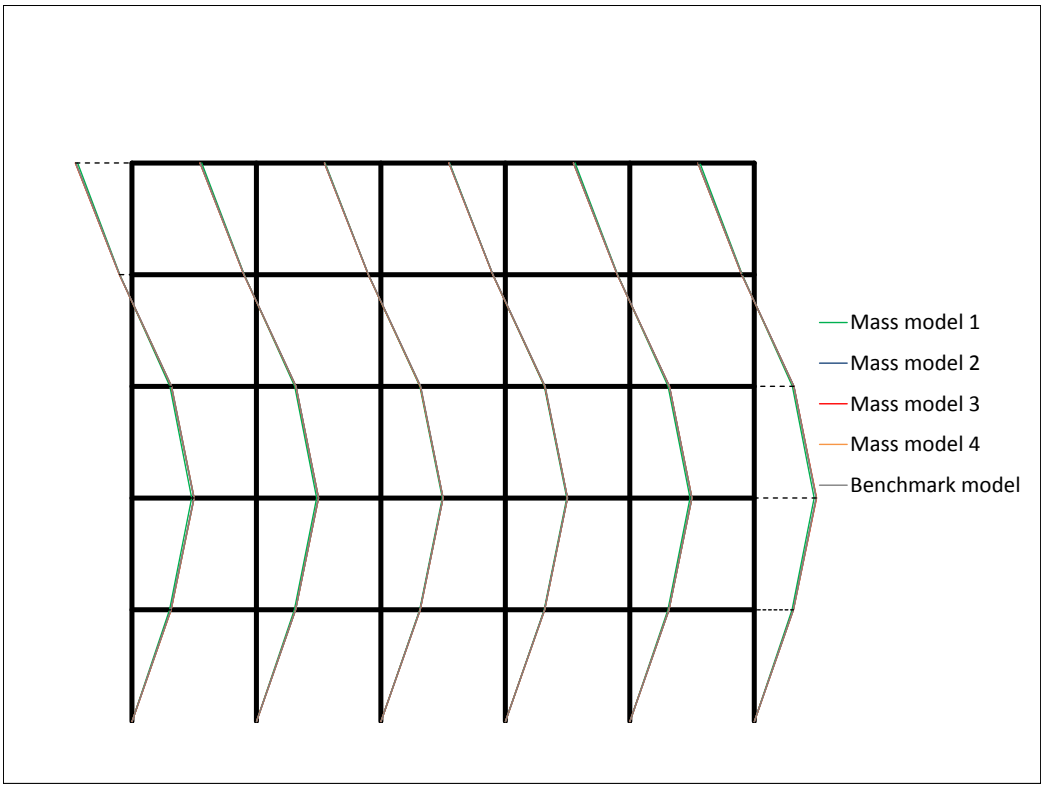

(b)

Figure 7.2.1: Horizontal mode shapes. (a) Mode 1 (b) Mode 2.

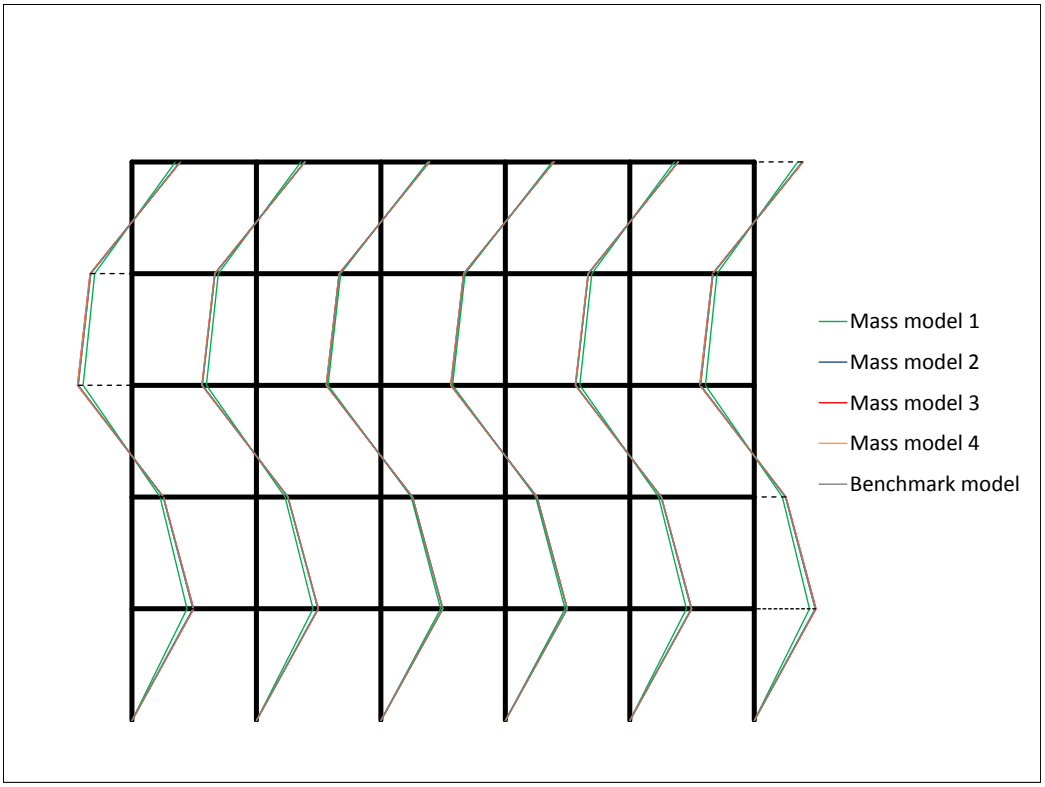

(a) Horizontal **mode 3**

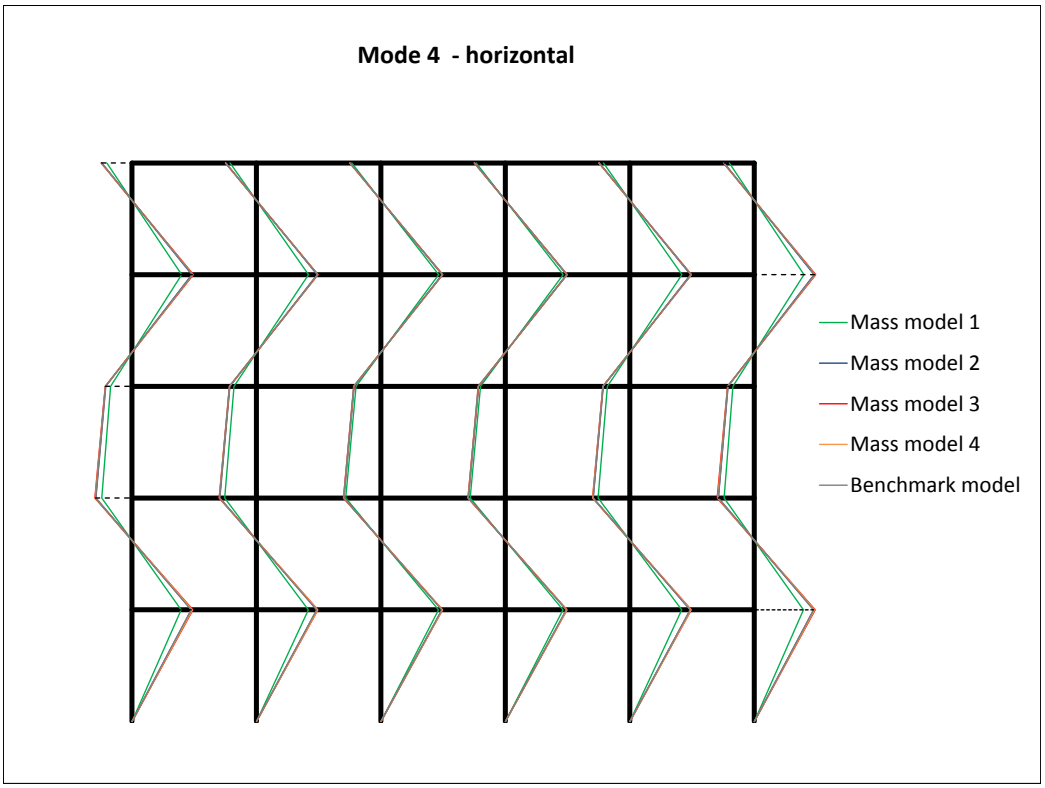

(b) Horizontal **mode 4**

Figure 7.2.2: Horizontal mode shapes. (a) Mode 3 (b) Mode 4.

Vertical modes:

Unlike the results for horizontal modes, there are remarkable differences from different mass models compared to the *Benchmark model* for vertical eigenvalues.

The vertical periods from Table 7.2.2 shows that the common lumped mass approach, *Mass model 1*, can lead to twice as high vertical periods as that of the *benchmark*. This applies to all vertical modes. All vertical mode shapes for *Mass model 1,* showed in Fig. 7.2.3 and 7.2.4, shows that the deformation pattern is completely different compared to the *benchmark* model. This implies that *Mass model 1* leads to unrealistic vertical deformations.

Compared to *Mass model 1, Mass model 2* is much more accurate to the *Benchmark*. However, there are clearly differences in the deformation pattern and periods. For all modes, Table 7.2.2 shows that *Mass model 2* has remarkably higher natural vertical periods than the *Benchmark model*. Furthermore, Fig. 7.2.3 and 7.2.4 shows that the accuracy of the natural vertical mode shape decreases for higher modes.

Mass model 3 and *Mass model 4,* in Fig. 7.2.3 and 7.2.4 and Table 7.2.2, shows both significantly similar periods and deformation pattern compared to the *Benchmark model*. Even though *Mass approach 3* has a coarse lumped mass approach compared to the *Benchmark model*, the eigenvalue comparison of this model to the *Benchmark model* implies very similar tendencies. This applies to all vertical modes. Moreover, differences in *Mass approach 3* and *Mass approach 4* are very small.

Based on the eigenvalue analysis, both *Mass model 3* and *Mass model 4* showed very high accuracy in both vertical mode shapes and periods compared to the *Benchmark model*. However, because of the small differences in *Mass model 3* compared to *Mass model 4*, *Mass model 3* is the coarsest simplified lumped mass model to cover realistic vertical motion with minimum computational effort.

Table 7.2.2: Vertical natural periods.

	Natural period, T_n (sec.)			
	Mode 1	Mode 2	Mode 3	Mode 4
Mass model 1	0.182	0.144	0.140	0.137
Mass model 2	0.089	0.087	0.083	0.081
Mass model 3	0.072	0.069	0.065	0.059
Mass model 4	0.076	0.073	0.068	0.061
Benchmark model	0.076	0.073	0.067	0.060

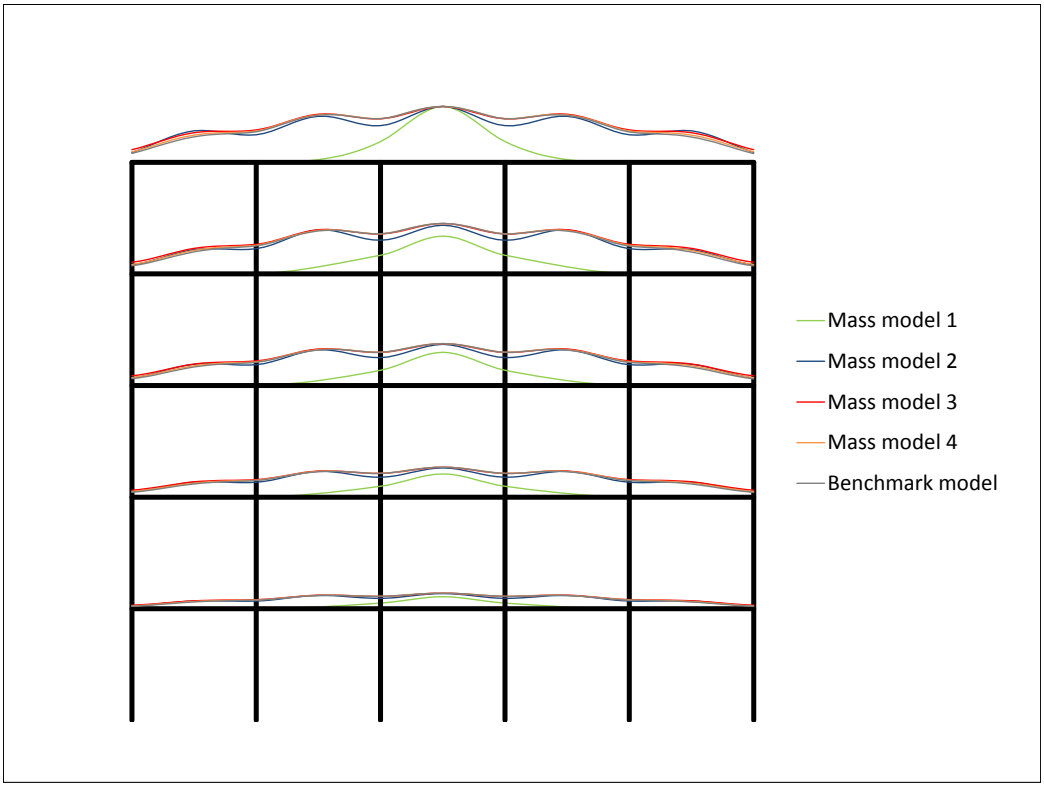

(a)

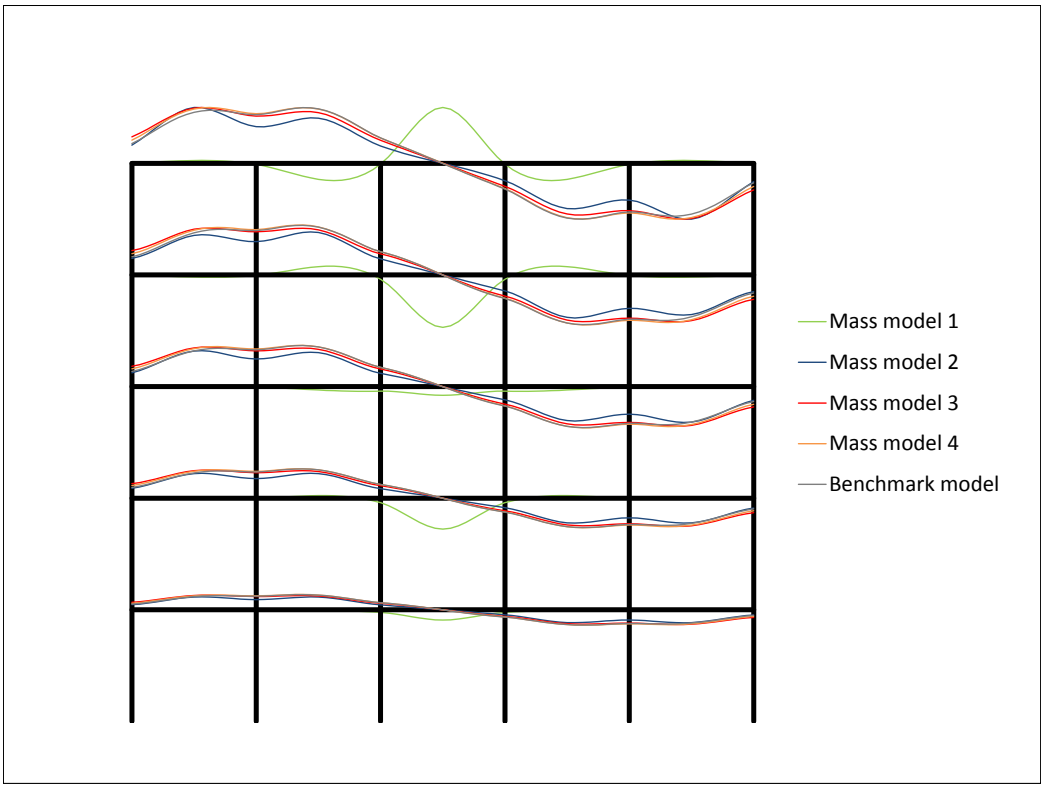

(b)

Figure 7.2.3: Vertical mode shapes. (a) Mode 1 (b) Mode 2.

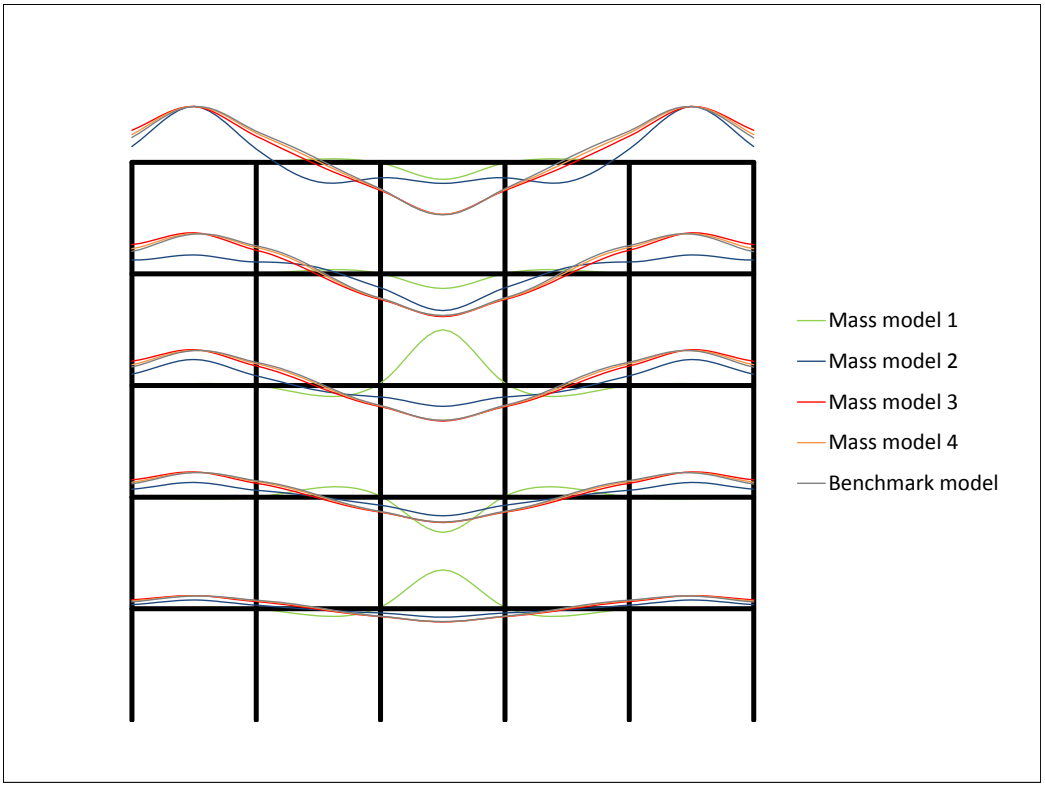

(a)

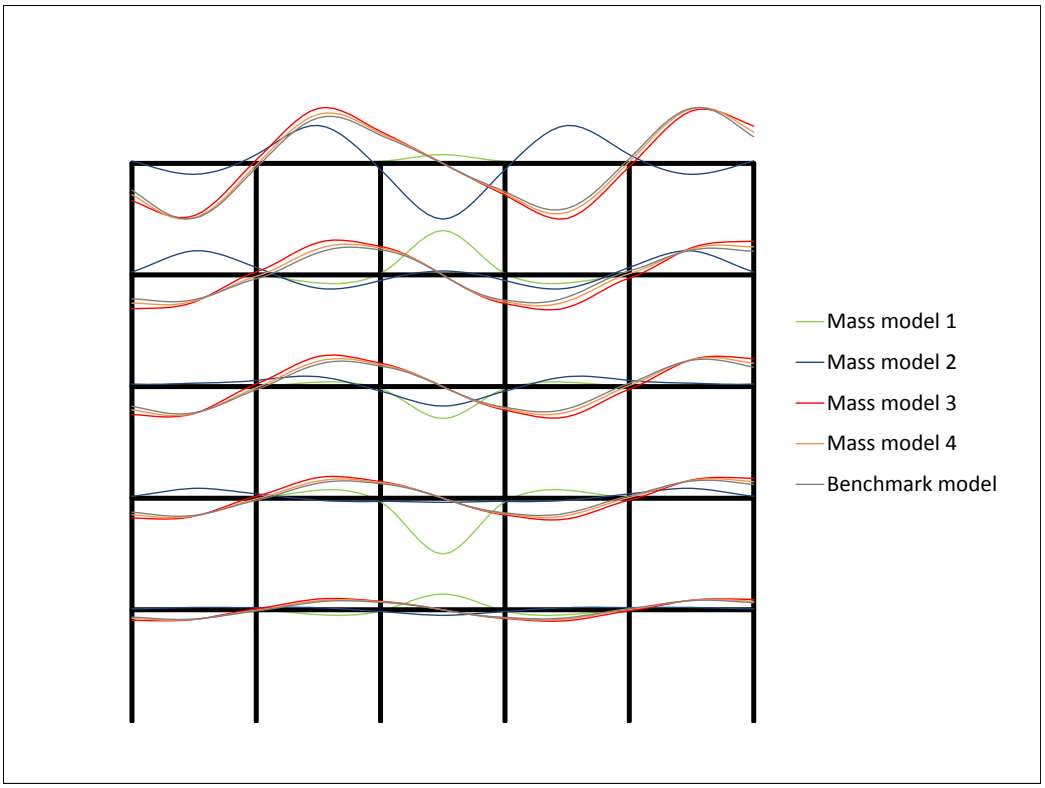

(b)

Figure 7.2.4: Vertical mode shapes. (a) Mode 3 (b) Mode 4.

7.2.2 Time history analyses

This section introduces time history analyses performed in this thesis. Time history analyses are performed on all simplified models and the benchmark model of the 2D building in Fig. 7.1.1. The intention of time history analyses are primary to evaluate response parameters in simplified models and compare them to response parameters in the *Benchmark model*. This verifies the accuracy of each model.

Time history analyses are solved by Eq. (3.2.1) under a set of both horizontal and vertical ground motions. This has been done in OpenSEES and Newmark's integration method is used. *Unconditional stability* in Newark's method are satisfied, were $\beta = 0.25$ and $\gamma = 0.5$. Furthermore, 5% damping is assumed and Rayleigh damping is used to calculate the damping matrix. The first horizontal mode and the first vertical mode, for each individual model, is used to calculate a_1 and a_2, respectively. Time step Δt of the recorded accelerations are $0.02s$ for all stations. The duration of the ground accelerations used are between 50 and 80sec.

Ground motion records

Recorded ground motions from the Christchurch earthquake February 2011 are used in the time history analysis. The earthquake had a magnitude of 6.3 (M) and the epicenter was centred 2 kilometers west of the town of Lyttelton, and 10 kilometers south-east of the center of Christchurch. Location of the epicenter and ground motion stations is showed in Fig. 7.2.5. Information about each station can be found in Table .

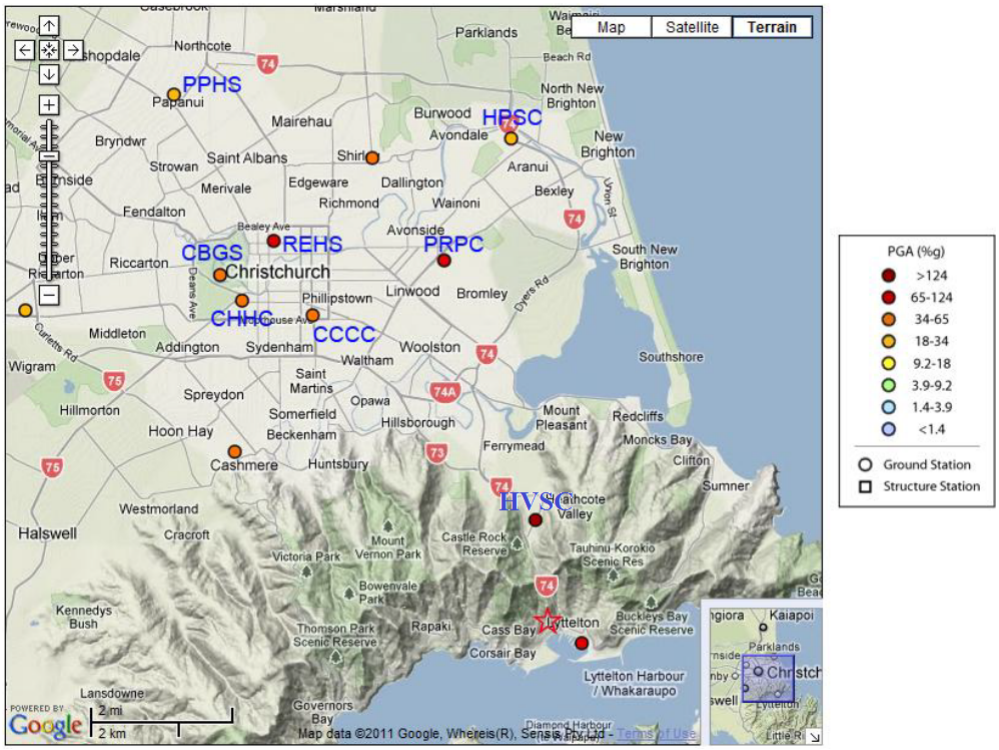

Figure 7.2.5: Map of the city of Canterbury and locations of the stations-

Ground motion records for eight of the most centered stations around the city are included in the analysis and both horizontal and vertical component are used.

The ground motion records are showed in Figures 7.2.6. These ground motions are used because of the high amplitudes of the vertical component of the ground motion. This is assumed to give a better basis when different lumped mass models are compared to the *Benchmark model*. As the ground motions shows, all vertical amplitudes are very strong and some of them are much stronger compared to the horizontal amplitudes. The red lines in all subfigures of Fig. 7.2.6 implies the vertical ground acceleration, and the blue lines the horizontal.

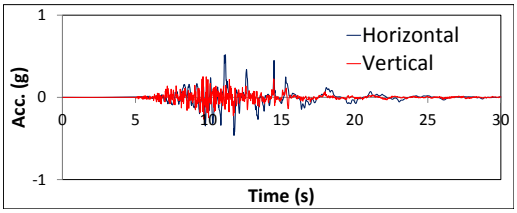

(a) CBGS station.

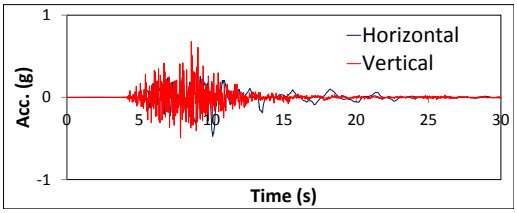

(b) CCCC station.

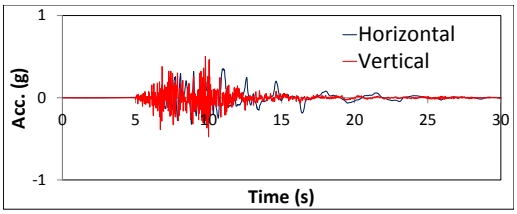

(c) CHHC station.

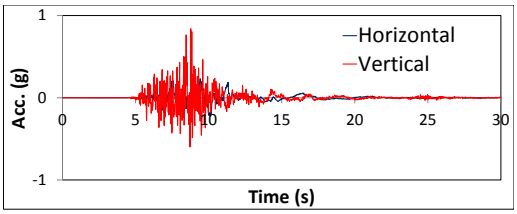

(d) HPSC station.

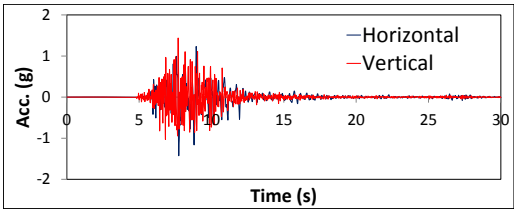

(e) HVSC station.

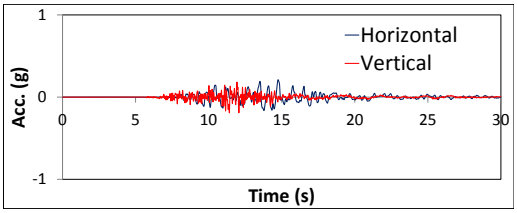

(f) PPHS station.

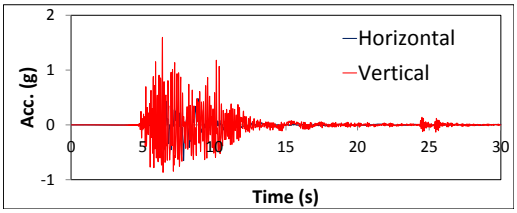

(g) PRPC station.

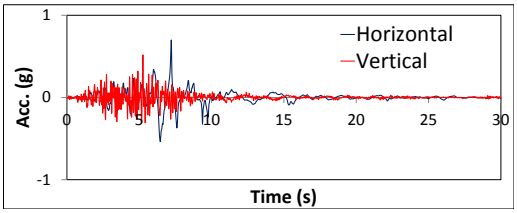

(h) REHS station.

Figure 7.2.6: Horizontal and vertical ground accelerations from the Christchurch earthquake.

Table 7.2.3: List of the earthquake records used in the numerical time history analysis.

Record nr.	Station	Epicentral Distance (km)	Comp.	PGA (g)
1	Cristchurch Cathedral College (CCCC)	6.0	$N64E$ UP	0.479 0.691
2	Cristchurch Reshaven (REHS)	8.0	$S88E$ UP	0.719 0.528
3	Papanaui High School (PPHS)	12.0	$S33W$ UP	0.213 0.195
4	ulverstone Drive Pumping (HPSC)	9.0	$S86W$ UP	0.294 0.857
5	Page Road Pumping (PRPC)	6.0	W UP	0.670 1.629
6	Cristchurch Botanic Gardens (CBGS)	9.0	$N89W$ UP	0.554 0.270
7	Cristchurch Hospital (CHHC)	8.0	$S89W$ UP	0.365 0.511
8	Heathcote Valley Primary School (CCCC)	2.5	$N64E$ UP	1.430 1.440

Comparative response of different models

Solutions of time history analyses are response parameters such as accelerations, shear forces and axial forces showed in Fig. 7.2.7. Due to symmetry properties, axial forces are determined in the three base column and shear forces in the end of the bottom beams. Accelerations are determined in the middle of each beam. Green points represents acceleration, blue line represent shear in the end of the lower beams and red lines represents axial forces in the base columns. Locations of shear and axial response parameters are chosen because these are normally fragile under earthquakes. Acceleration response location is strategically positioned in the middle of each beam to obtain highest vertical acceleration in the building.

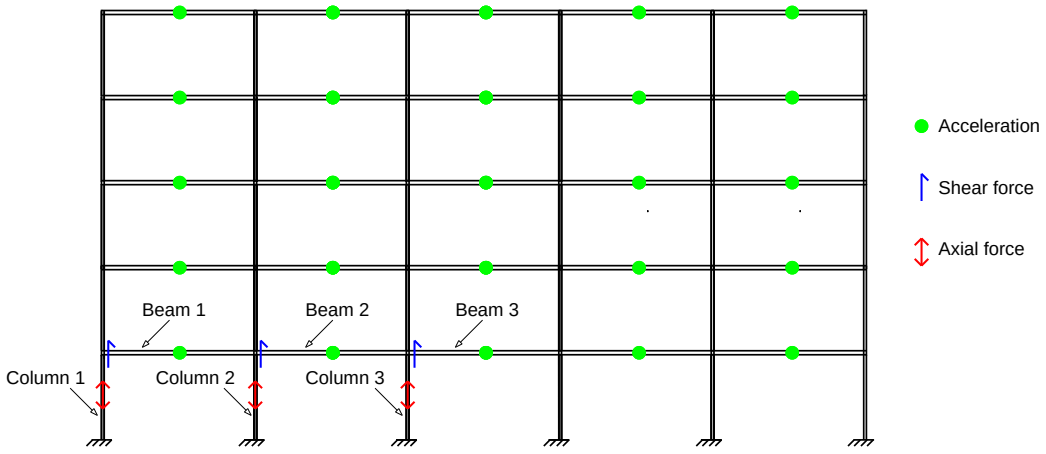

Figure 7.2.7: Response parameters of the time history analysis. Green points are acceleration, blue lines are shear forces and red lines are axial forces.

In each model, the maximum response parameters from each ground motion determines

from time history analysis. Then, the maximum responses of all eight ground motions are added and then divided by eight. This gives the average response parameters from all eight ground motions of each model. Furthermore, to evaluate the response parameter errors from each simplified model compared to *Benchmark model*, the following equation are used

$$Model\ error = \left(\frac{Response\ of\ Mass\ model\ i}{Response\ of\ The\ becnchmark} - 1 \right) * 100\%$$

where i = *Mass model 1, 2, 3* and *4.*

This shows the percentage error for each model compared to the *Benchmark model.*

7.2.3 Time history analysis results

The results from the time history analysis gives the total error of each simplified model compared to the *Benchmark model,* because both vertical and horizontal component of the ground motion are used in the analysis.

Each response parameter errors are provided in separate figures.

Discussion of acceleration errors

The Y-axis in Fig. 7.2.8 represent each floor level in Fig. 7.2.7. The X-axis represents negative or positive errors compared to the *Benchmark Model.* Positive errors implies higher acceleration response, and negative implies lower. For simplicity's reasons, the acceleration error is the average acceleration error in each floor.

The entire discussion is based on Fig. 7.2.8 unless stated otherwise.

Mass model 1: Mass model 1 shows between 19% to 45% less acceleration compared to the *Benchmark model.* The acceleration errors are smallest in the lower floor, and increases for each floor. This, however, are the common trend for all mass models.

Mass model 2: Mass model 2 is much more accurate than *Mass model 1* compared to the *Benchmark model.* However, the accelerations are up to 10% less for the higher floors. On the other hand, the acceleration in the first floor shows that *mass model 2* gives 9% more acceleration compared to the *Benchmark model.*

Mass model 3 and 4: Conservative results appears when the acceleration errors of *Mass model 3 and 4* are compared to the *Benchmark model.* Although both models shows very small errors, the errors implies more acceleration in each and single floor. This implies that *Mass model 3 and 4* contributes to higher acceleration in each floor than the *Benchmark model.*

Based on acceleration errors in Fig. 7.2.8, both *Mass model 3 and 4* showed low errors compared to the *Benchmark* and can reasonably capture the effects of vertical ground motion. Moreover, because the errors between these models are small, the coarsest, *Mass model 3,* can simulate the effects of vertical ground motions with reliable accuracy and least amount of computational effort.

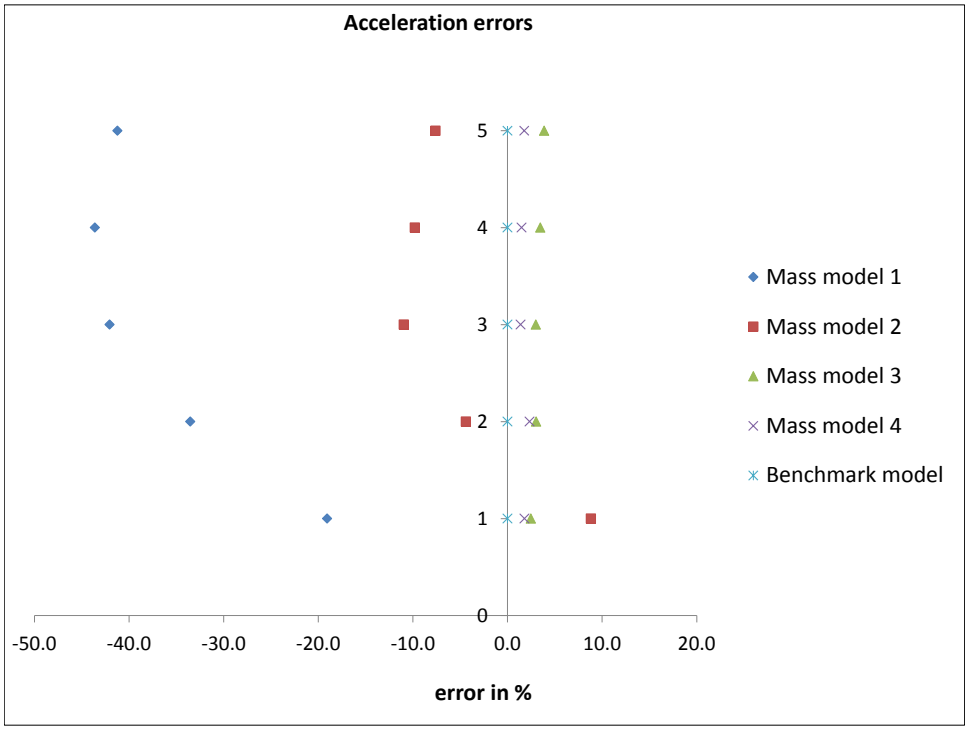

Figure 7.2.8: Acceleration errors for each model compared to the *Benchmark model*. x=0.0 implies the *Benchmark model*.

Discussion of shear forces

The X-axis in Fig. 7.2.9 represents the lower beams from Fig. 7.2.7 from beam 1 to beam 3. The Y-axis represents positive and negative shear force errors for each mass model compared to the *Benchmark model*. Negative shear force errors implies less shear force compared to the *Benchmark model* and positive shear force implies more.

The entire discussion is based on Fig. 7.2.9 unless stated otherwise.

Mass model 1: The shear force errors of *Mass model 1* shows that it is over 70% more shear force in the inner beam while there are very low otherwise compared to the *Benchmark model*. High shear forces in the inner beam comes from that the mass in this model are centered only in the middle of each floor.

Mass model 2: Mass model 2 shows that it is more shear forces in all beams compared to the *Benchmark model*. The biggest positive errors are 7% in the inner beam.

Mass model 3: Mass model 3 shows that it is less shear forces in all beams compared to the *Benchmark model*. However, the negative errors are less than 6% in all beams.

Mass model 4: Mass model 4 shows that it is slightly more shear forces in all beams compared to the *Benchmark model*. However, the negative errors are less than 2% in all beams

Based on the shear force errors in Fig. 7.2.9, *Mass model 1* is useless to simulate realistic shear force effects from vertical ground motion, *Mass model 2, 3* and *4* shows accurate tendencies. However, only *Mass model 4* is very accurate compared to the *Benchark model*.

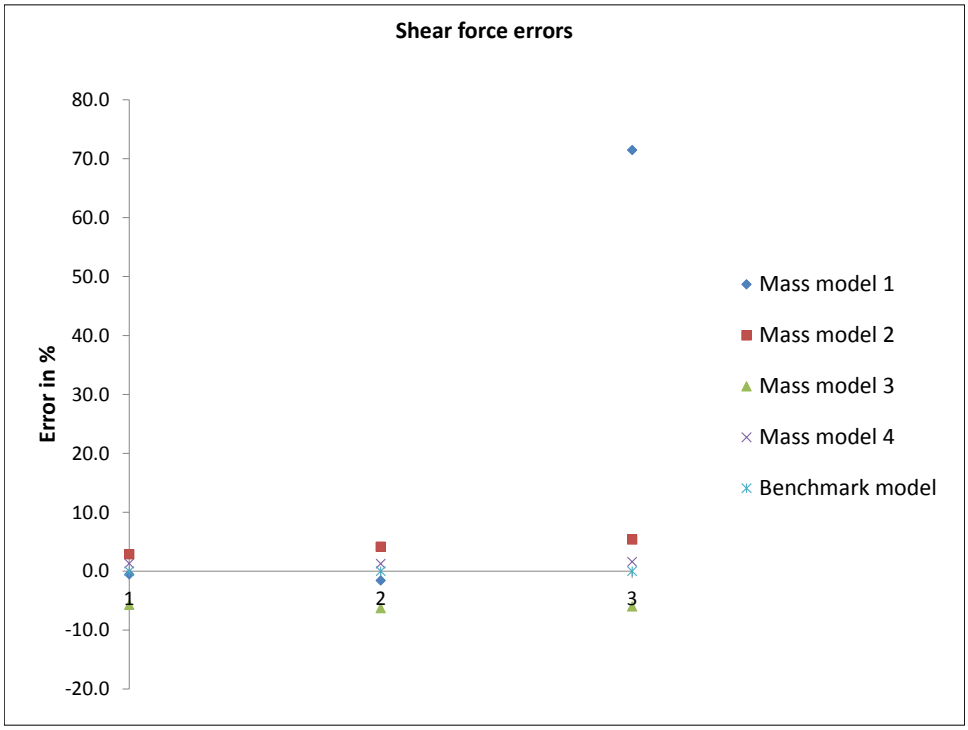

Figure 7.2.9: Shear force errors for each model compared to the *Benchmark model*. y=0.0 implies the *Benchmark model*.

Discussion of axial forces

The X-axis in Fig. 7.2.10 and 7.2.11 represents the base columns showed in Fig. 7.2.7. The Y-axis represents positive and negative axial force errors for each mass model compared to the *Benchmark model*. Negative axial force errors implies less axial force compared to the *Benchmark model* and positive force implies more. Fig. 7.2.10 and 7.2.11 shows compressive and tensile forces, respectively.

The entire discussion is based on Fig. 7.2.10 for compressive and Fig. 7.2.11 for tensile, unless stated otherwise.

Mass model 1: Both compressive and tensile forces in *Mass model 1* shows negative errors in column 2 and the errors are between 80 and 100% compared to the *Benchmark model*. Similar for the inner column, although here there are positive errors of 60% and 50%. Furthermore, the outer column shows 9% negative errors in compressive and 5% positive errors in tensile.

Mass model 2: Mass model 2 shows up to 17% positive compressive force errors compared to the *Benchmark model* while tensile force errors are low for all columns.

Mass model 3: Mass model 3 shows small errors in compressive, but significantly higher in tensile. In tensile, the error is at is maximum of 20% negative in the inner column compared to the *Benchmark model*. In compressive, the maximum error is 8% negative.

Mass model 4: Mass model 4 shows very small errors compared to the *Benchmark model*. Errors from both tensile and compressive forces are less than 3%.

The most accurate mass model compared to the *Benchmar model* is *Mass model 4*. Both tensile and compressive errors are here very low. Nevertheless, even if *Mass model 3* shows some differences, this model needs considerably less computationally efforts than *Mass model 4*. Taken all analysis methods into account, *Mass model 3* shows small errors and differences to the *Benchmark model*.

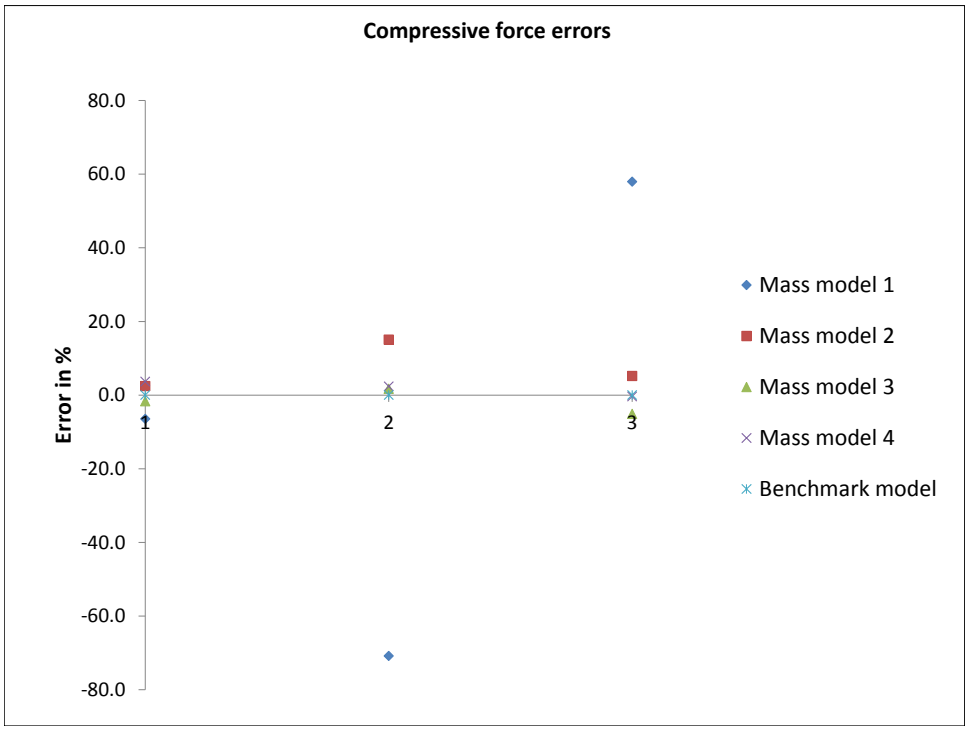

Figure 7.2.10: Compression force errors for each model compared to the *Benchmark model*. y=0.0 implies the *Benchmark model*.

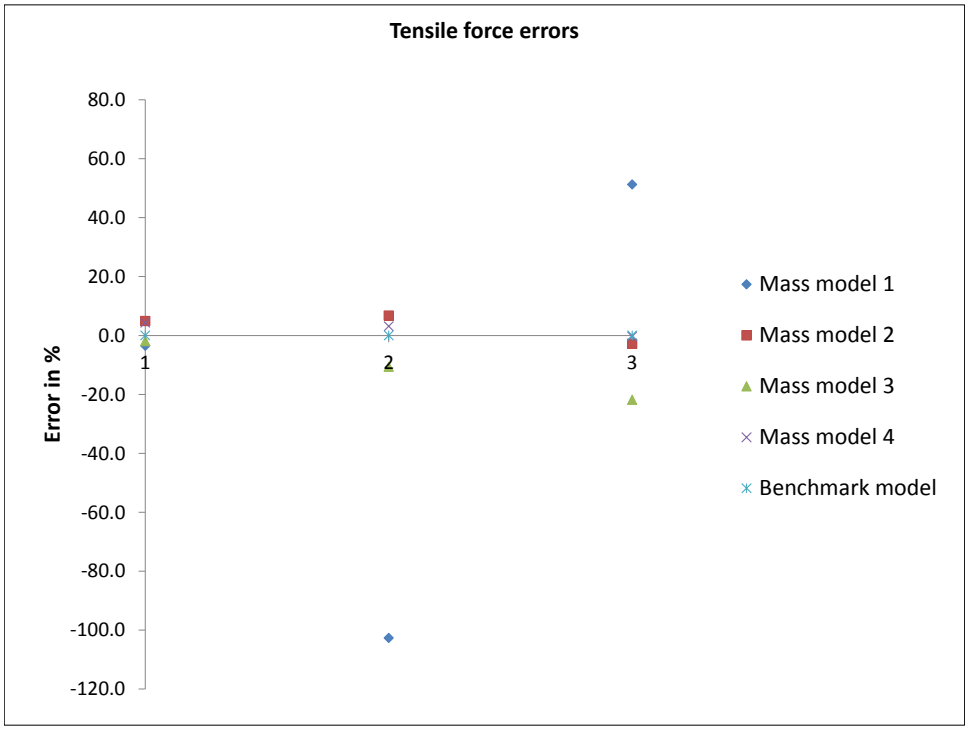

Figure 7.2.11: Tension force errors for each model compared to the *Benchmark model*. y=0.0 implies the *Benchmark model*.

Based on both eigenvalue analysis and time history analysis, *Mass model 3* and *4* are simplified models which had overall small differences and small errors compared to the *Benchmark model*. However, terms to take into account is that the computational effort is twice as less in *Mass model 3* compared to *4*.

Chapter 8

3D Modeling, Analyses, Results and Discussion

8.1 Introduction of the building

Similar to the building modelled in 2D, a fairly common building is modelled 3D. Fig. 8.1.1 shows 3D view of the building. The building is assumed to be reinforced concrete. A preliminary design to determine column, beam and slab sites were conducted. Properties of the building is to be found in Table 8.1.1 and Fig. 8.1.2 sizes the building's overall dimensions at each elevation and plan view.

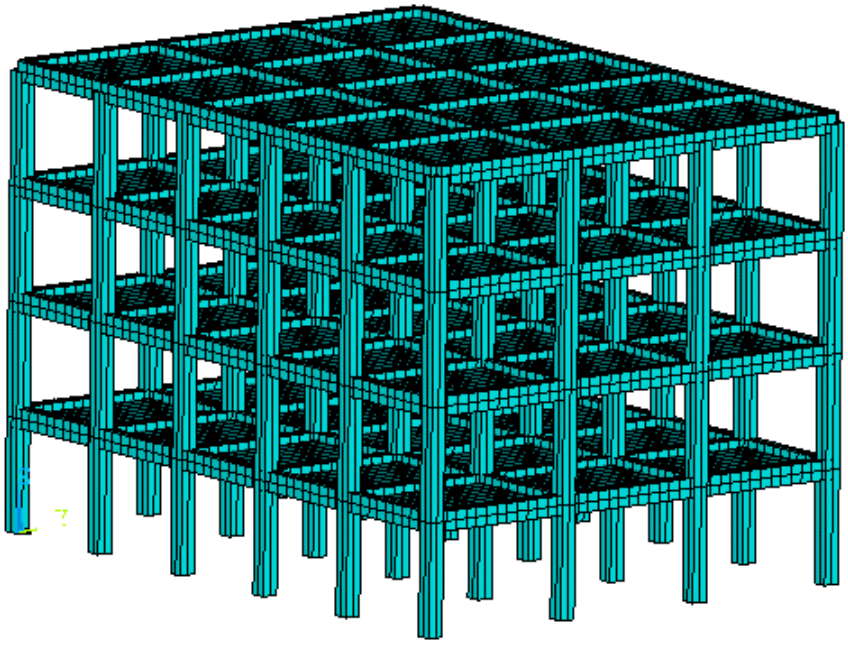

Figure 8.1.1: 3D view of the four story building. All structural members are modelled as elastic.

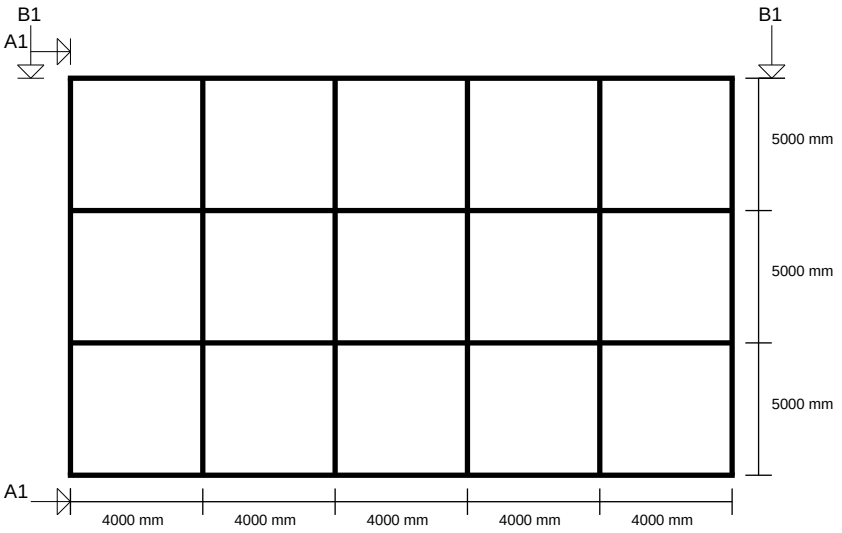

(a) Plan view.

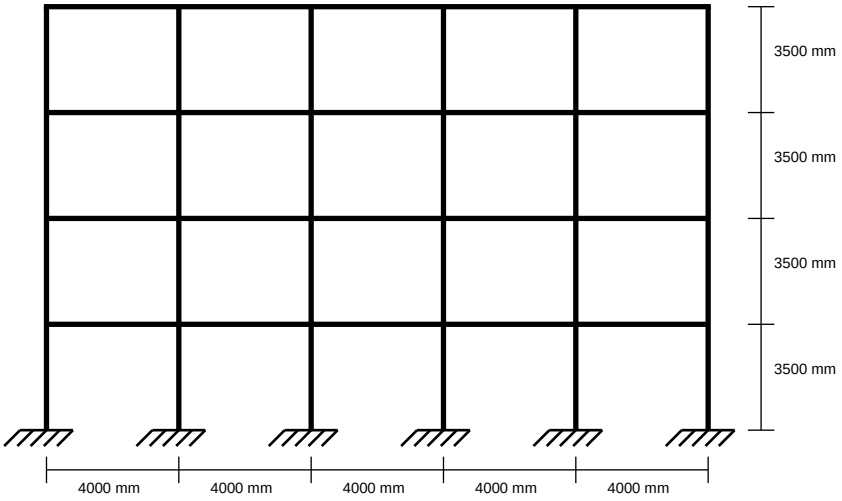

(b) Section B-B.

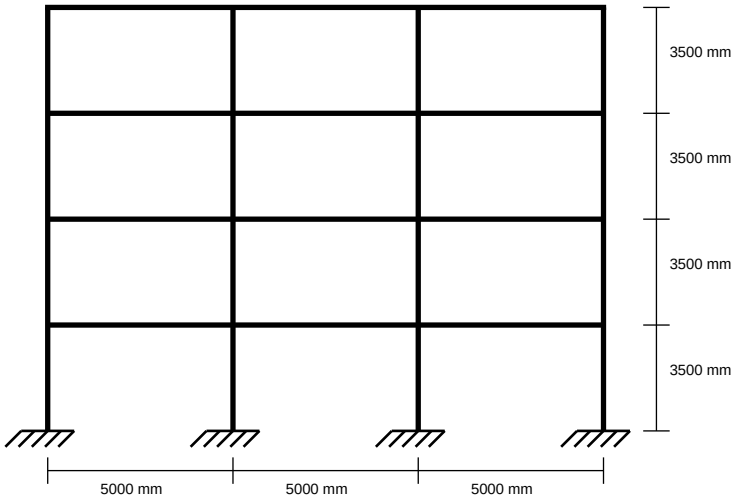

(c) Section A-A.

Figure 8.1.2: Sections of the Building. (a) Plan view (b) Section A-A (c) Section B-B.

Both OpenSEES and ANSYS are used to model this building. To serve as the *exact* solution, a highly refined element mesh over the slab is created in ANSYS where the consistent mass approach is used. Shear deformation effects are included in the *exact* model.

Several alternative models are developed in OpenSEES. First of all, the building is modeled using the common, rigid-diaphragm approach where the slab is assumed to possess in-plane stiffness. Later, slabs are physically modeled using shell elements. Two different mesh configurations are used to identify the optimum solution which can capture the vertical effects without compromising simplicity. Beam and columns are modeled using Bernoulli beams. All shear deformations are neglected.

Table 8.1.1: Structural Properties for the 3D building.

Properties	Initials	Values
Cross section beams and Girders	$H_b \cdot B_b$	$600\,mm \cdot 400\,mm$
Cross section Columns	$H_c \cdot B_c$	$500\,mm \cdot 500\,mm$
Slab thickness	S_T	$150\,mm$
Young-module	E	25000
Poisson's ratio	ν	0.18
Mass at each floor	M_i	387 $tons$
Total mass including	M_{tot}	1548 $tons$

8.1.1 The benchmark model

The *Benchmark model* is created in ANSYS and the slab is modeled with 1500 shell elements over each floor, as shown in Fig. 8.1.3. Shell element are based on Mindlin plate theory and shear deformations are included. Furthermore, columns are modeled with one Bernoulli beam element per structural member.

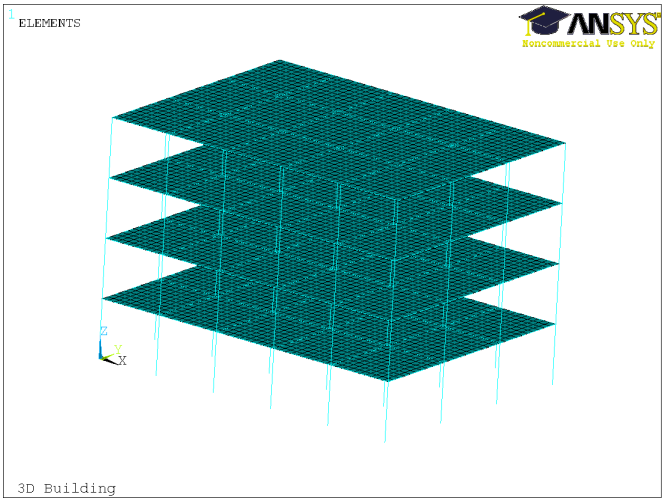

Figure 8.1.3: The *benchmark model* in ANSYS. Each floor includes 1500 shell elements.

8.1.2 Simplified lumped mass models

The intention is now to model the slab explicit with an optimum number of shell elements and mass configuration and compare the Eigen-values and eigen-vectors with to the *Benchmark model.*

Fig. 8.1.4a shows plan view of the building modeled using the common rigid-diaphragm approach, where the slab is assumed to possess in-plane stiffness. This model is called *Rigid diaphragm model.*

Fig. 8.1.4b shows a plan view of the finest shell element mesh with lumped mass assigned to all nodes. This model is called *Shell model 240*, because 240 shell elements are used to mesh the slab in each floor.

Fig. 8.1.4c shows a plan view of the coarsest shell element mesh with lumped mass assigned to all nodes. This model is called *Shell model 60,* because 60 shell elements are used to mesh the slab in each floor.

Other simplified models are not provided to model the slab. However, it is to mention that beam elements was tried to be included, but highly unrealistic deformation pattern and periods was observed and therefore not included in this thesis.

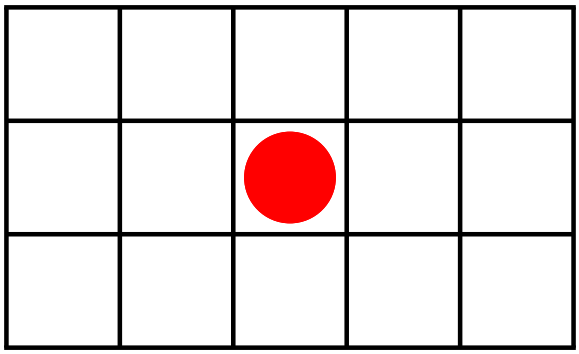

(a) *Rigid diaphragm model*

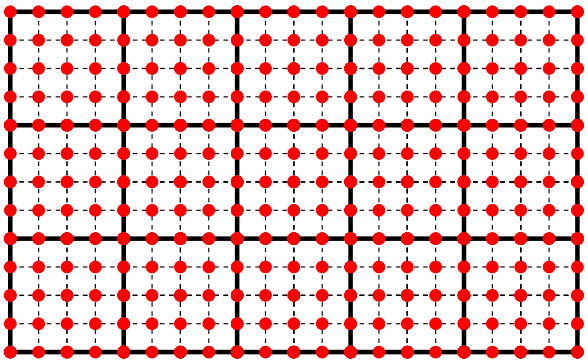

(b) *Shell model 16*

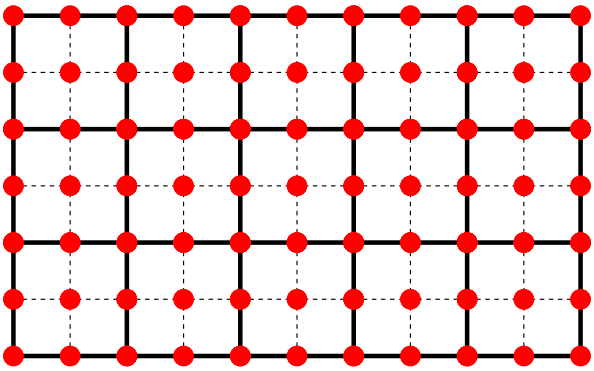

(c) *Shell model 4*

Figure 8.1.4: Lumped mass models in 3D. One red point implies one lumped mass. (a) *Rigid diaphragm model* (b) *Shell model 16* (c) *Shell model 4*.

8.2 Eigenvalue analyses 3D

The first three modes in each direction is obtained by eigenvalue analyses in OpenSEES and ANSYS. Similar for 2D, all mode shapes from all models are plotted on top of each other to show differences in between models and to compare simplified models to the *Benchmark model*. The mode shapes are normalized with the quantity 1.0 at the top of the roof for each mode.

Due to the symmetrical properties of the building, vertical mode shapes are plotted for sections A1-A3 to A3-A3 and B1-B1 to B3-B3 as shown in Fig. 8.2.1. Horizontal mode shapes are plotted for each elevation view, vertical mode shapes for section A-A and B-B in Fig. 8.1.2 and torsional mode shapes are plotted in the plan view where only the upper floor of the building are used.

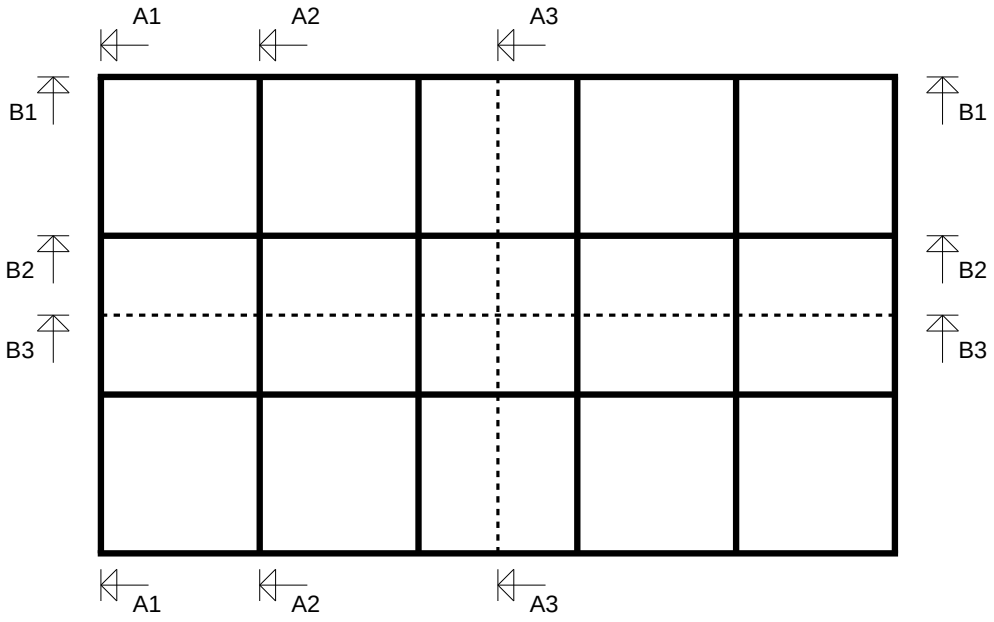

Figure 8.2.1: Sections A1-A1 to A6-A6 and B1-B1 to B4-B4 of the 3D building. Dashed lines implies center lines of each section.

Natural horizontal and torsional mode shapes and vibrations periods are presented and discussed first.

Discussion of horizontal and torsional modes

The following discussion is drawn from natural horizontal mode shapes in Fig 8.2.2, 8.2.3 and 8.2.4 and natural horizontal periods in Table. 8.2.1. The green lines represents the *Benchmark model,* yellow line represents the *Rigid diaphragm model,* red line represents *Shell 240 model* and blue line represents *shell model* 60. Dashed lines in all figures represents the building in undeformed state.

Discussion

Table 8.2.1 shows that there are small differences of horizontal and torsional periods regardless of which model is used compared to the *Benchmark model*. This applies for all modes. However, *Shell model 60* shows biggest differences in periods compared to the *Benchmark model*. That applies for all modes in all directions, which implies that *Shell model 60* is stiffer in horizontal motion compared to the *Benchmark model.*

Table 8.2.1: Horizontal and Torsional natural periods.

		Natural periods (sec)		
Mode shape direction	Model	Mode 1	Mode 2	Mode 3
Horizontal A-A	*Benchmark model*	0.543	0.175	0.102
	Rigid diaphragm model	0.548	0.176	0.101
	Shell model 16	0.533	0.172	0.100
	Shell model 4	0.513	0.167	0.099
Horizontal B-B	*Benchmark model*	0.506	0.166	0.099
	Rigid diaphragm model	0.509	0.166	0.098
	Shell model 16	0.498	0.163	0.097
	Shell model 4	0.483	0.160	0.096
Torsional	*Benchmark model*	0.439	0.143	0.084
	Rigid diaphragm model	0.425	0.138	0.080
	Shell model 16	0.443	0.145	0.085
	Shell model 4	0.411	0.135	0.081

Fig. 8.2.2, 8.2.3 and 8.2.4 shows zero or extremely small differences of the horizontal mode shapes for all simplified models in all directions and in all modes compared to the *Benchmark model.*

Based on the horizontal eigenvalue results, all of the simplified models can obtain realistic horizontal motion. Therefore, the *Rigid diaphragm model* can obtain realistic horizontal mode shapes and periods with least amount of computational effort.

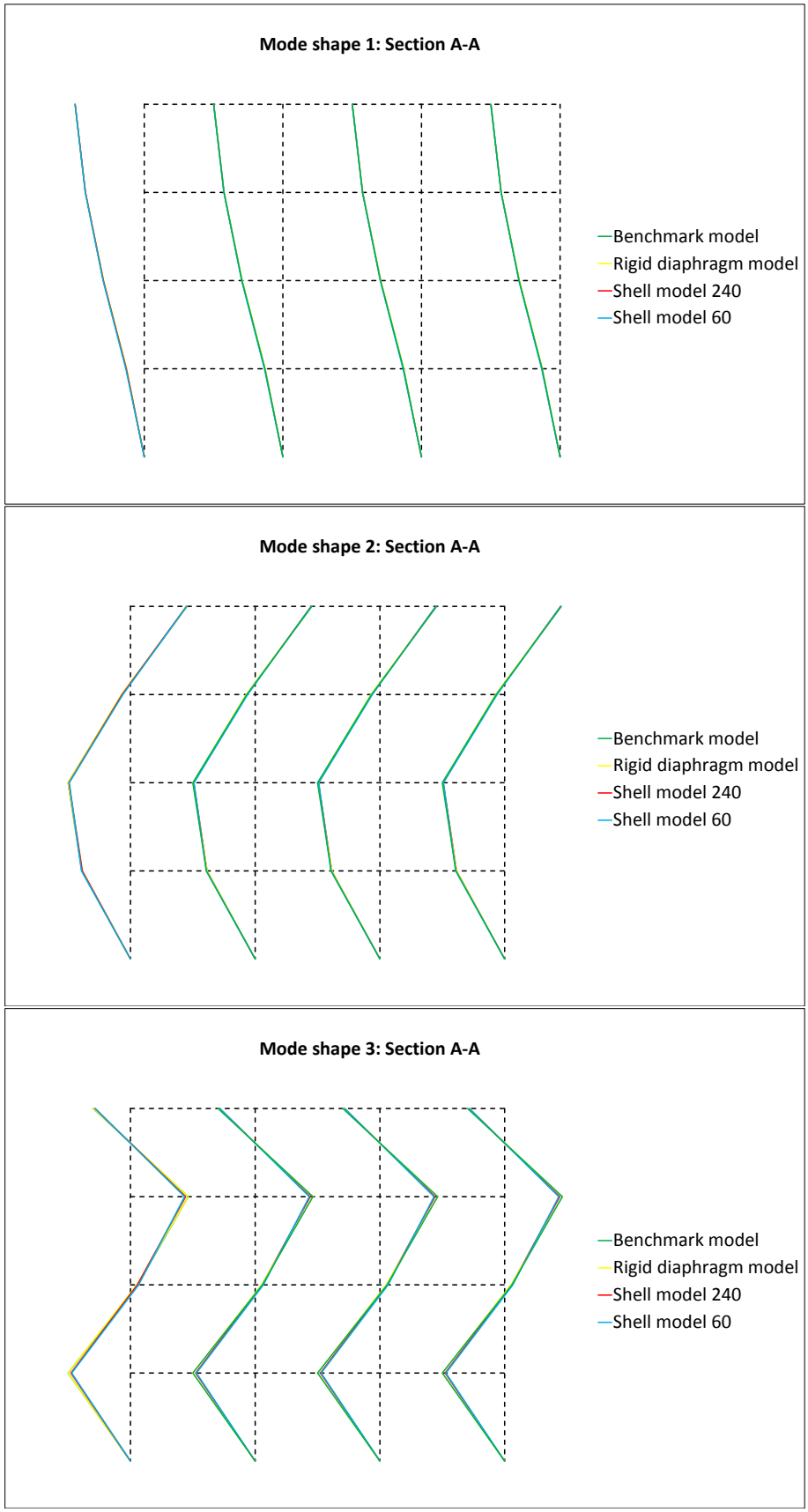

Figure 8.2.2: Horizontal mode shapes section A-A.

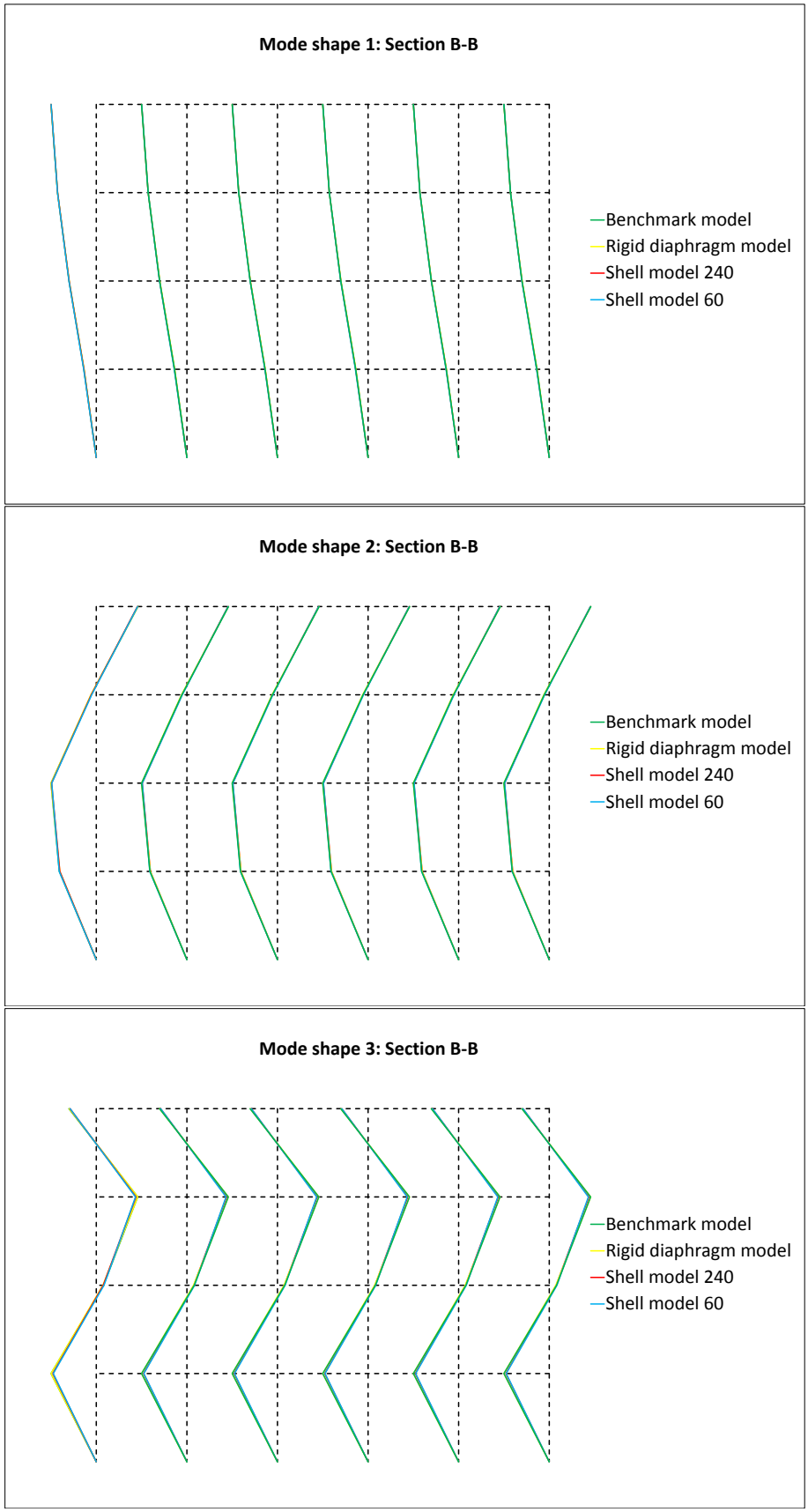

Figure 8.2.3: Horizontal mode shapes section B-B.

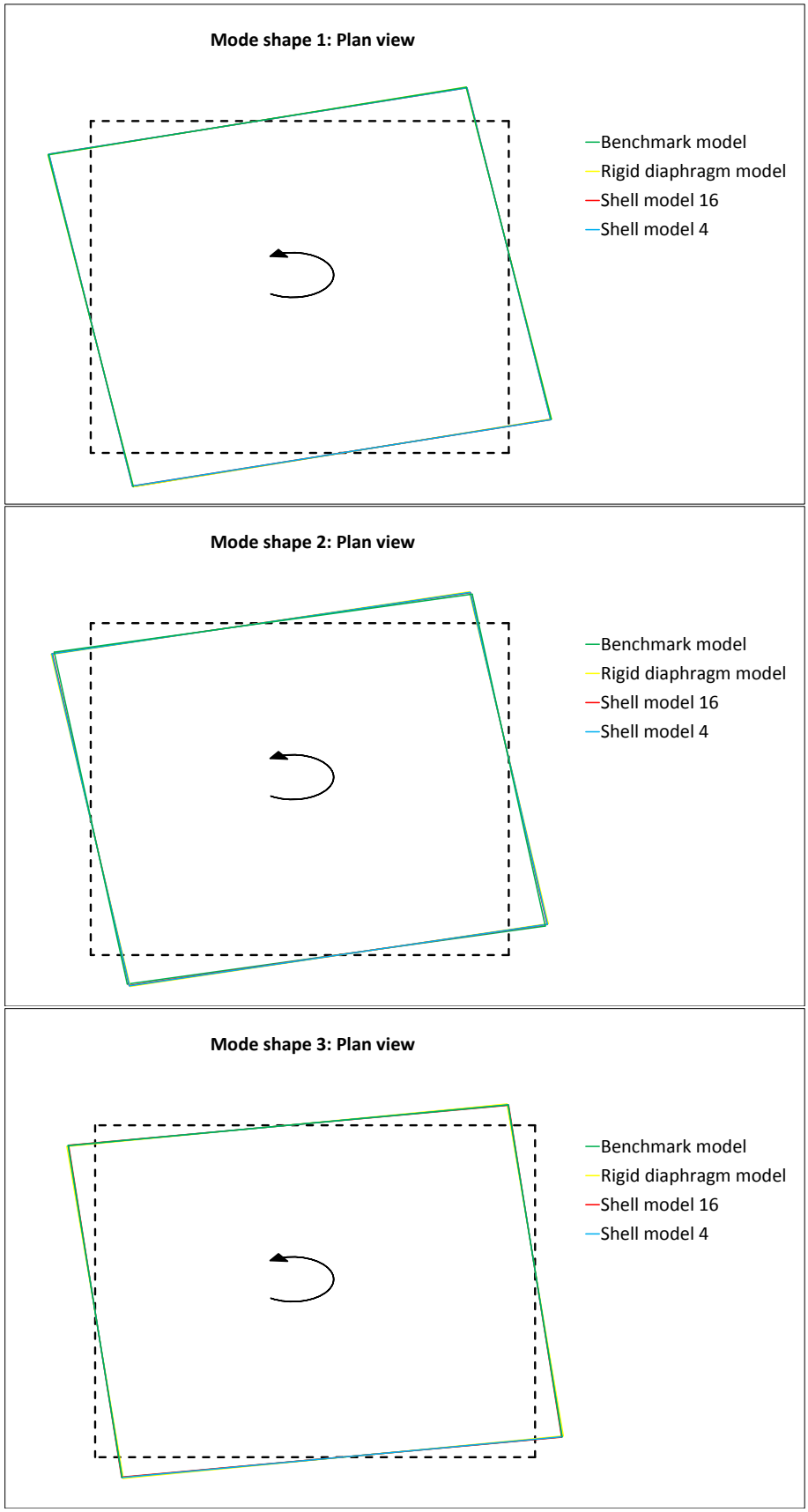

Figure 8.2.4: plan view of torsional mode shapes for the upper floor.

Discussion of vertical modes

The following figures shows natural vertical mode shapes from section A1-A1 to A3-A3 or B1-B1 to B3-B3. There are in total 6 figures. Furthermore, the first two figures shows all sections of vertical mode 1, then the next two figures shows all sections for vertical mode 2, and the two last figures shows all sections for vertical mode 3.

Discussion

As opposed to the horizontal modes, there are clearly differences in the vertical mode shapes for different models. First of all, Table 8.2.1 shows that there are no vertical periods obtained by the *Rigid diaphragm model.* Furthermore, *Shell model 240* shows very small differences in the vertical periods compared to the *Benchmark model* while there are some differences for *Shell 60.* Regardless of mode, the differences in between models remain the same.

Table 8.2.2: Vertical natural periods.

		Natural period (sec)		
Direction	Model	Mode 1	Mode 2	Mode 3
Vertical	*Rigid diaphragm model*	-	-	-
	The benchmark model	0.075	0.073	0.071
	Shell model 16	0.073	0.071	0.069
	Shell model 4	0.067	0.063	0.060

The following discussion are based on Fig. 8.2.5, 8.2.6, 8.2.7, 8.2.8, 8.2.9 and 8.2.10.

Since the tendencies for all vertical mode shapes in all mode are the same, a general discussion of all figures follows immediately.

Rigid diaphragm: Yellow lines in all figures, which represent mode shapes of the *Rigid diaphragm model,* show zero vertical deformation pattern. There are no vertical modes.

Shell model 60: Red lines in all figures, which represents mode shapes of *Shell model 60,* shows that the vertical mode shape in mode 1 only follow the *Benchmark model* in a global context. There are clearly differences, but only in detail level. However, the differences reduces with higher modes and the vertical mode shapes are very much more accurate compared to the *Benchmark model.*

Shell model 240: Blue lines in all figures, which represents mode shapes of *Shell model 240,* shows that there are very small differences even in detail level compared to the *Benchmark model.* This appeals to all modes and all sections.

Vertical modes cannot be simulated or captured using a rigid diaphragm method. However, extremely similar mode shapes and very small differences in the periods compared to the *Benchmark model* indicates that *Shell model 240* can simulate vertical motion with great accuracy compared to the *Benchmark model.* However, *Shell model 60* showes overall similar mode shapes and followed the *Benchmark model* in the global context in all modes. General accurate similarities of *Shell model 60* compared to *Benchmark model* implies that *Shell model* 60 can simulate vertical motion with useable accuracy.

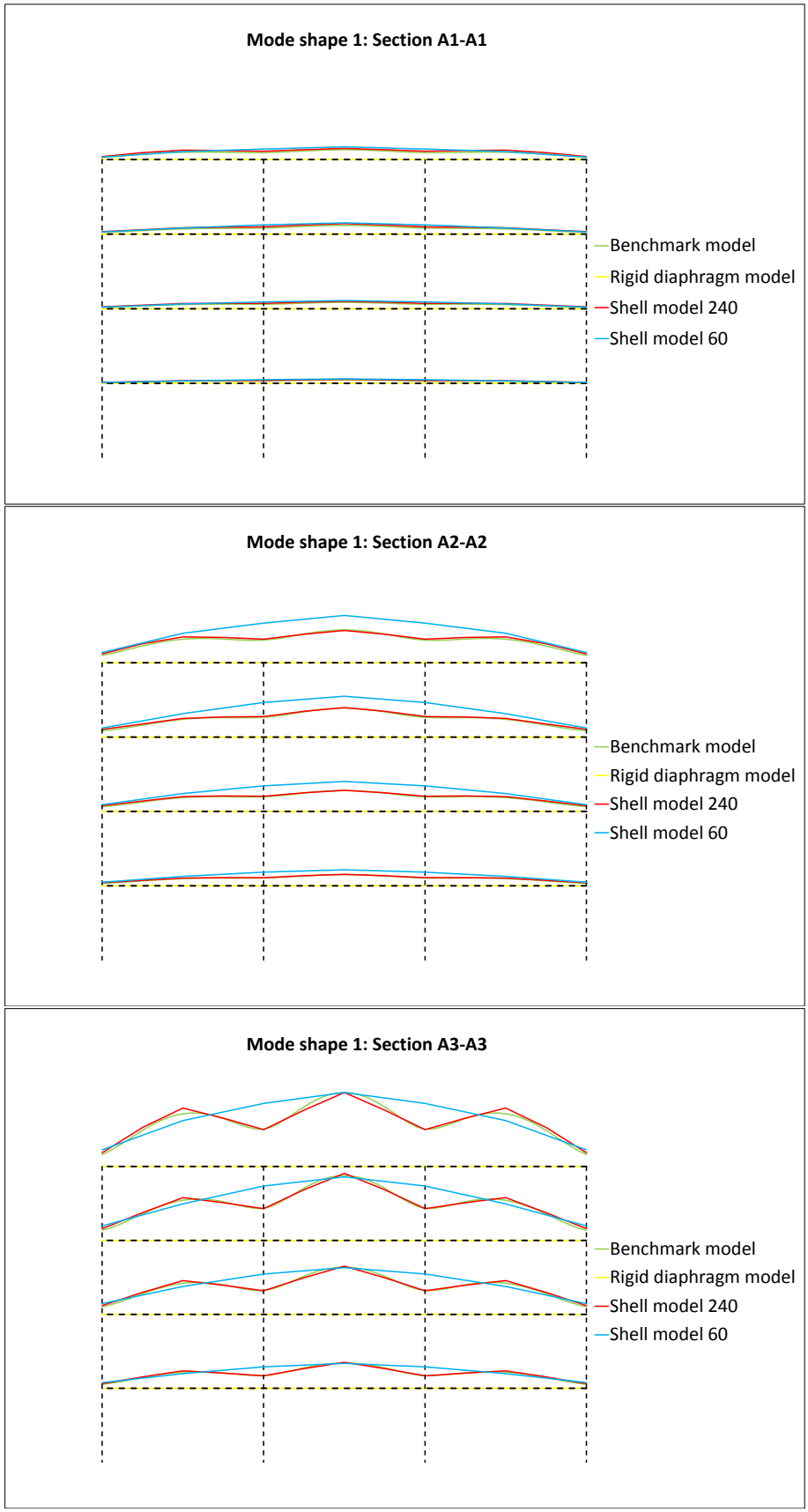

Figure 8.2.5: Vertical mode shape 1, section A1-A1, A2-A2 and A3-A3.

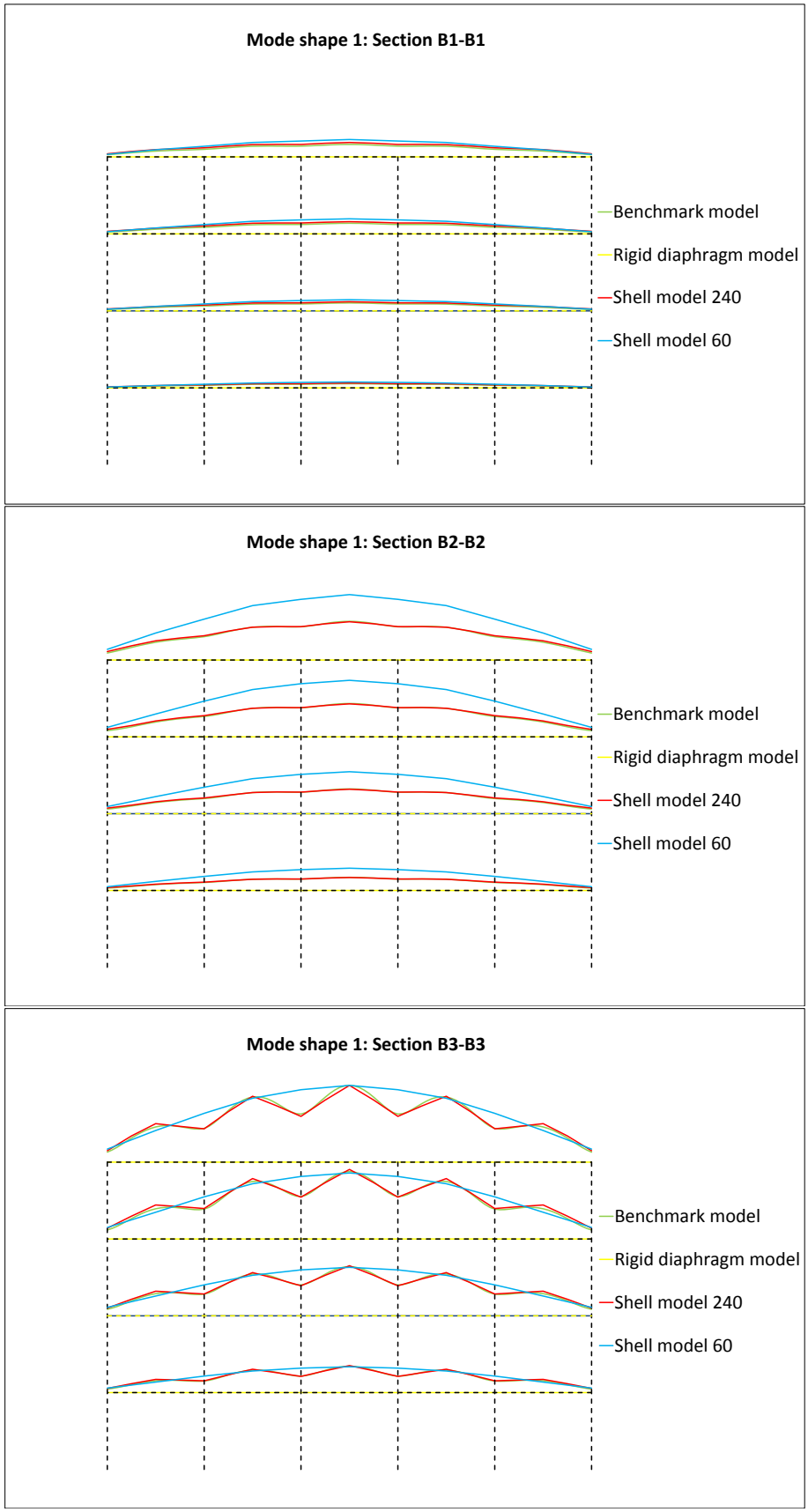

Figure 8.2.6: Vertical mode shape 1, section B1-B1, B2-B2 and B3-B3.

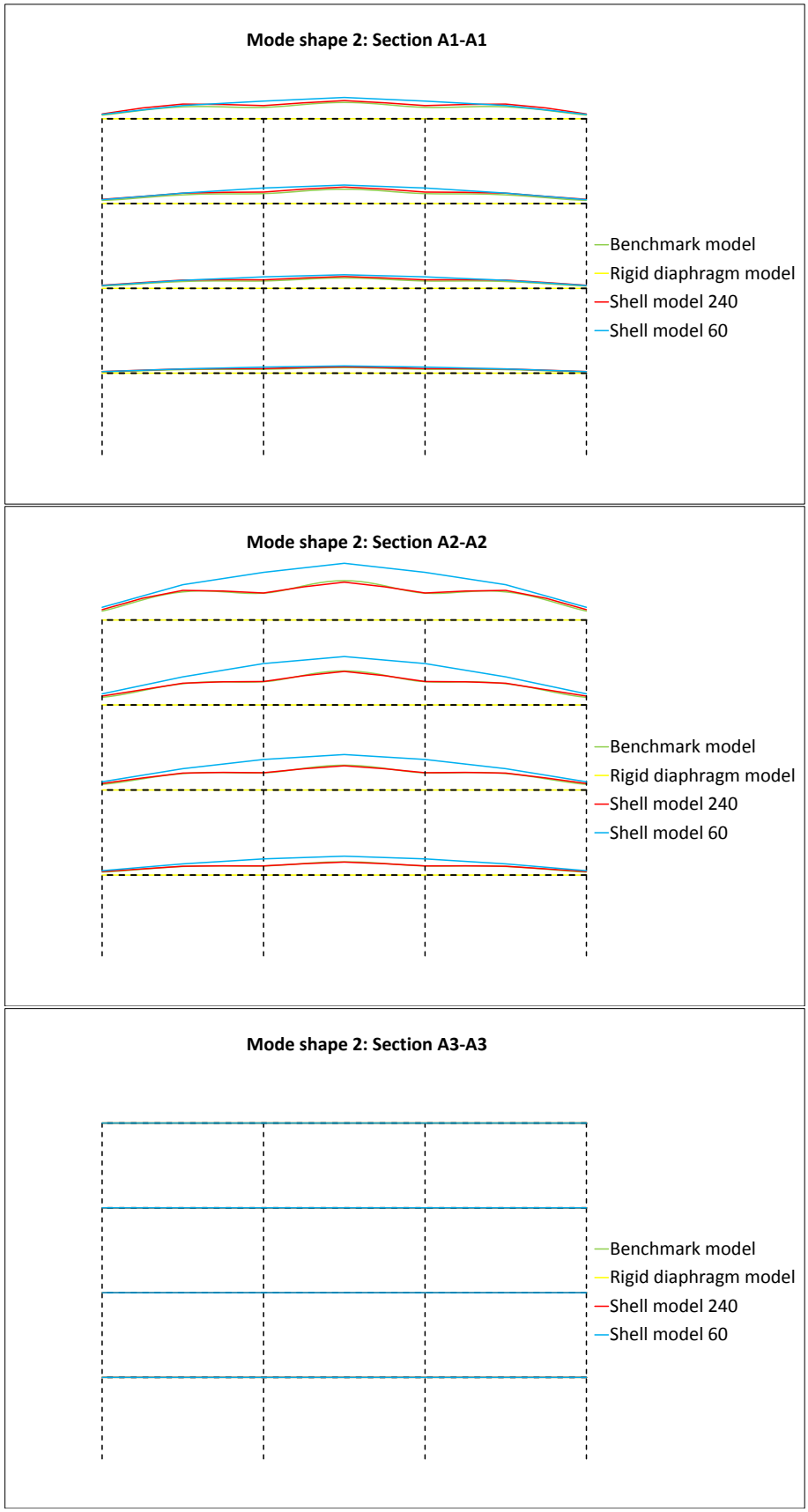

Figure 8.2.7: Vertical mode shape 2, section A1-A1, A2-A2 and A3-A3.

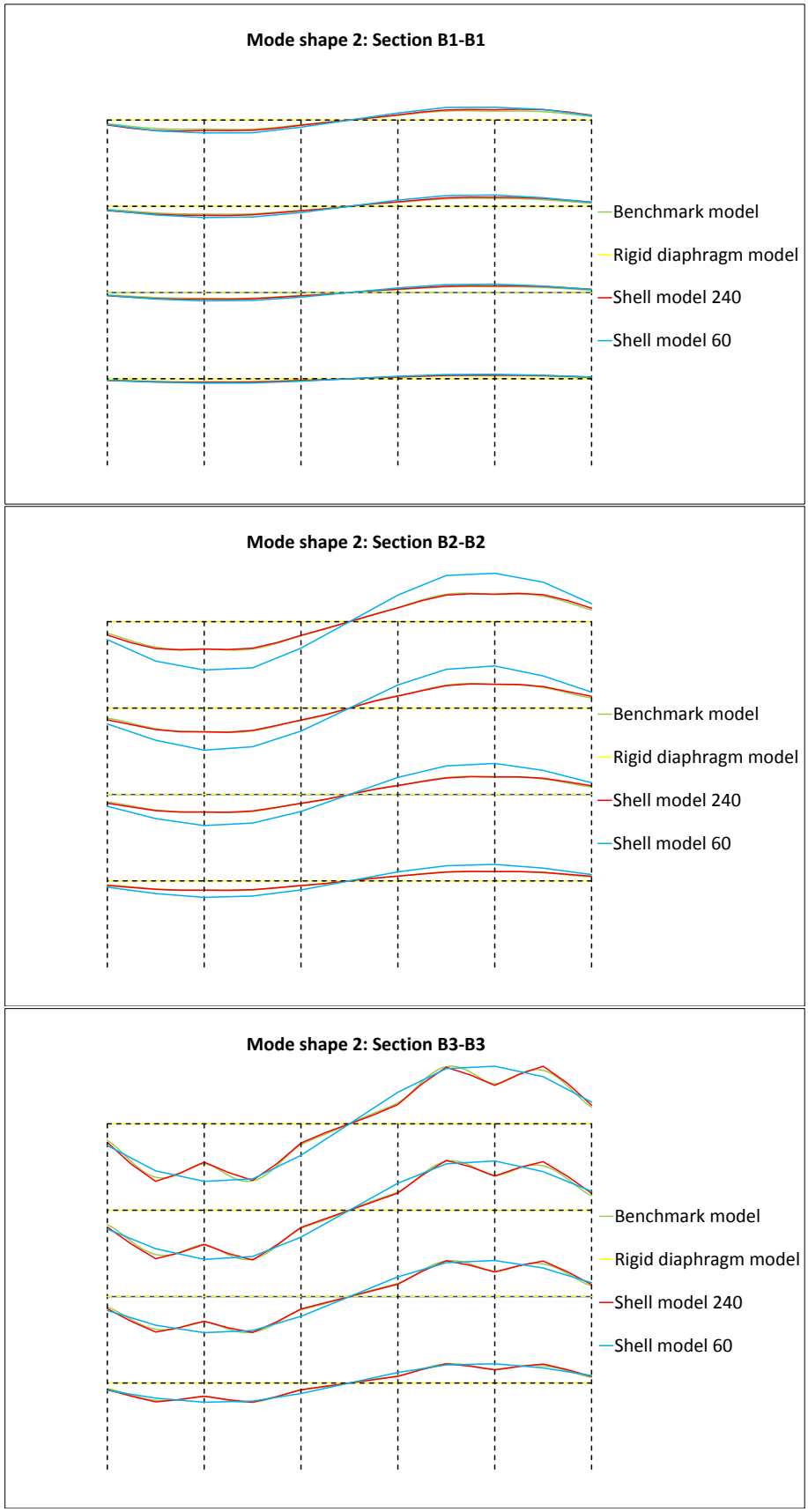

Figure 8.2.8: Vertical mode shape 2, section B1-B1, B2-B2 and B3-B3.

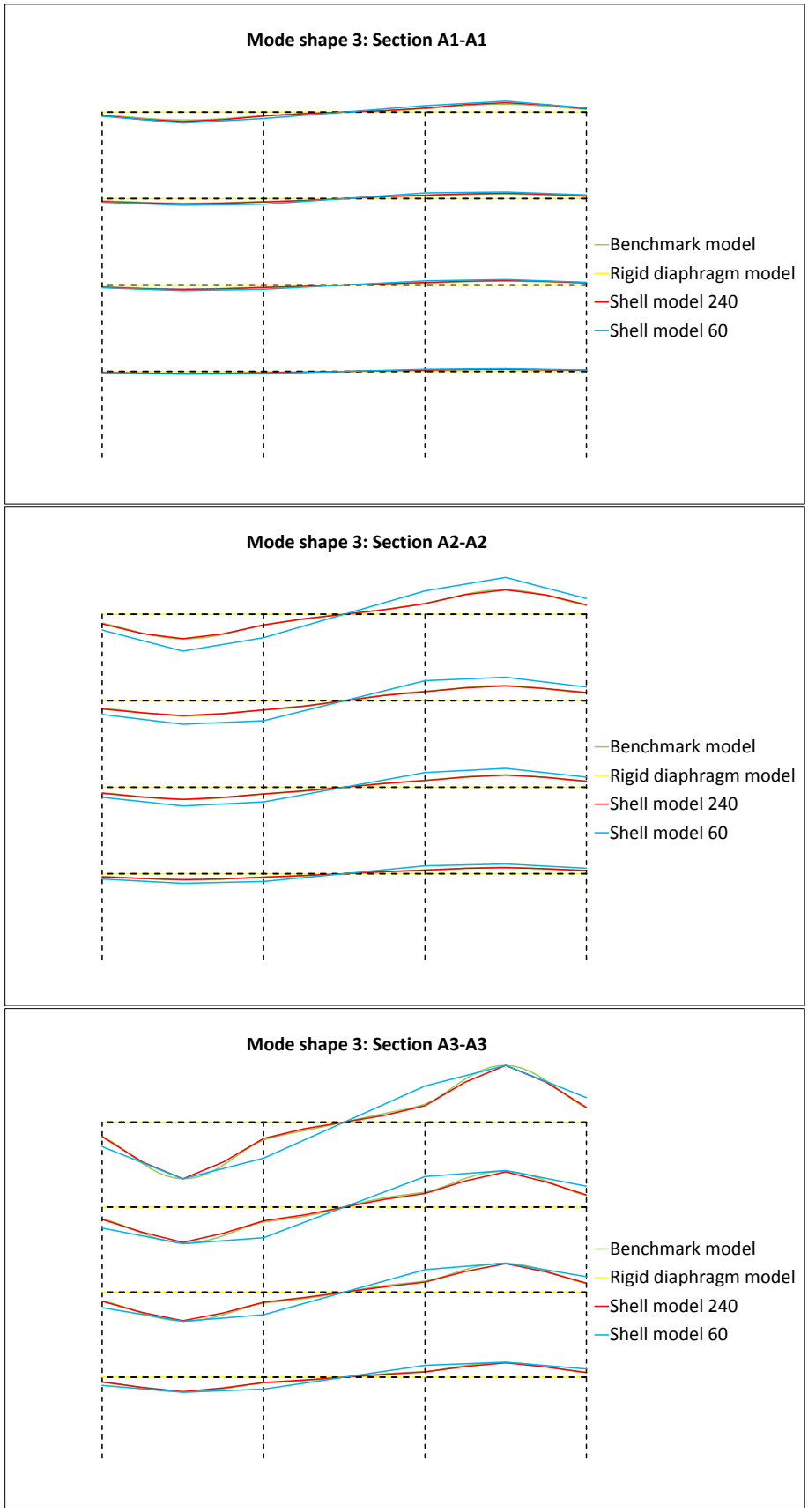

Figure 8.2.9: Vertical mode shape 3, section A1-A1, A2-A2 and A3-A3.

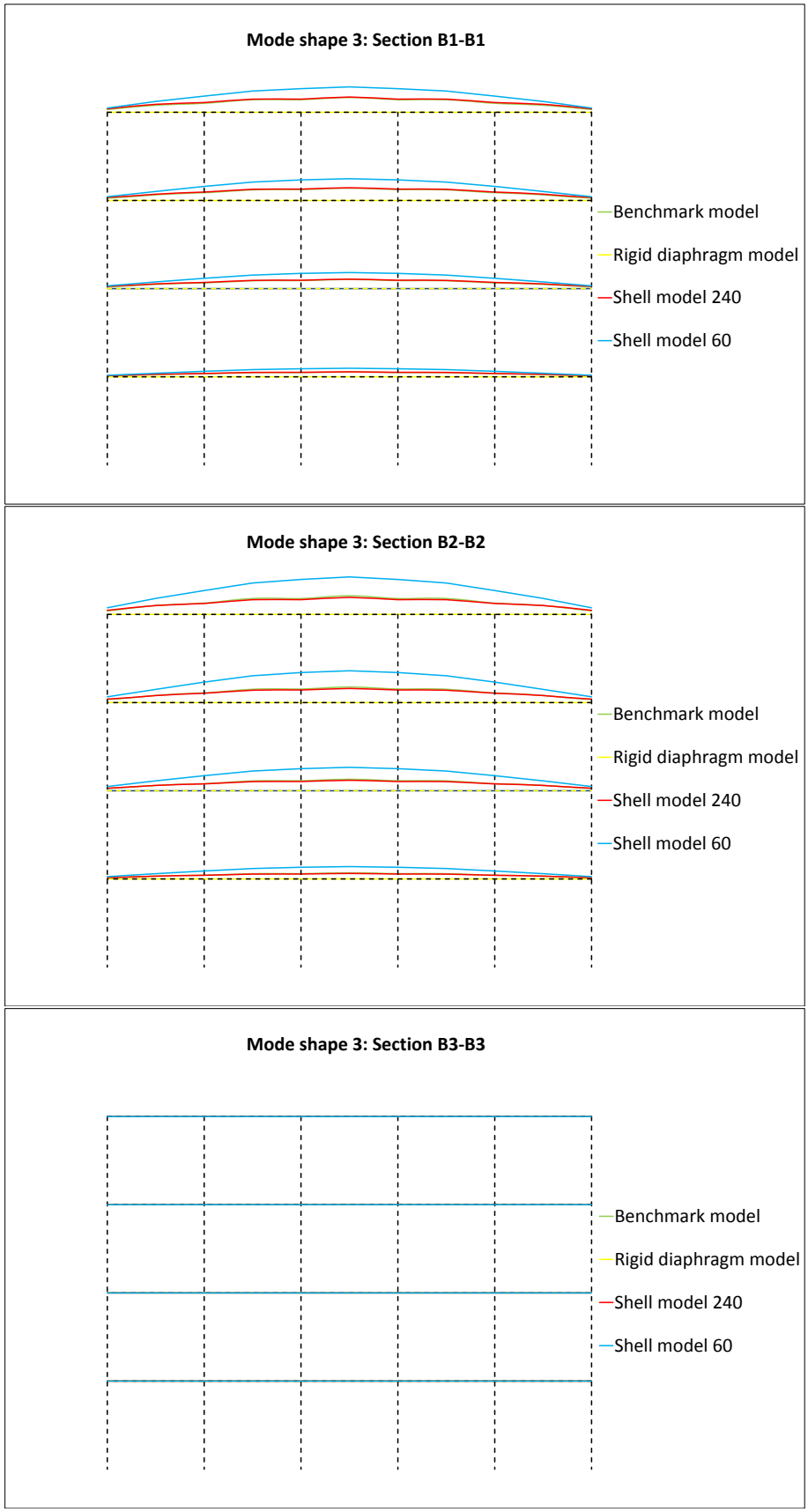

Figure 8.2.10: Vertical mode shape 3, section B1-B1, B2-B2 and B3-B3.

Chapter 9

Conclusion and Recommendations

9.1 Summary

With the increasing interest in vertical ground motions, modeling buildings to simulate the effects of vertical motions remains to be a major challenge for the earthquake engineering community. In this thesis, simplified modeling approaches are investigated to see if a lumped mass approximation could simulate the vertical motion realistically. This was done by comparing natural mode shapes and periods from the simplified models to an *exact* solution modeled with an extremely refined element mesh.

Solutions from eigenvalue analysis confirmed that the common modeling procedure could not be used to simulate realistic vertical motion. This applies especially to the common rigid diaphragm method. However, it was succeeded to create simplified lumped mass models with remarkable similarities of natural mode shapes and periods compared to *exact* solution in both 2D and 3D.

9.2 Conclusion and observations

The following conclusions are drawn from the evaluation of both eigenvalue analysis and time history analysis. However, evaluation of the time history analysis includes only the building modeled in 2D.

Simplified models in 2D

- *Mass model 1,* which is the common procedure to model buildings in earthquake engineering practice, showed that natural vertical mode shapes and vibration periods mismatched completely to the *Benchmark model*. The deformation patterns from the mode shapes showed very unrealistic behavior and got even worse for higher modes. Furthermore, the average acceleration level was up to 50% less and the axial and shear force at the inner columns up 100% more compared to the *Benchmark model*. Based

on this, *Mass model 1* cannot be used to simulate realistic vertical motion.

- *Mass model 2* showed small, but noticeable, differences in the first vertical mode shape and vibration period compared to the *Benchmark model*. For higher modes, the errors increased and was completely off for the fourth vertical mode shape. Results from the time history analysis showed that the acceleration level mismatched up to 10% to the *Benchmark model*. Furthermore, errors of shear and axial forces was 14%. Based on the noticeable errors compared to the *Benchmark model*, particularly in the mode shapes, *Mass model 2* is not suitable to simulate the dynamic behavior of buildings in the vertical direction.

- *Mass model 3 and 4* showed both significantly similar vertical mode shapes and periods to the *Benchmark model*. Time history analysis showed that *Mass model 3* had some errors of shear forces and axial forces compared to *Benchmark model* while *Mass model 4* showed in all response parameters less than 3% errors from the *Benchmark model*.

- *Mass model 3* require least amount of computational effort to simulate realistic vertical motion with reliable accuracy compared to the *Benchmark model*.

- All simplified models showed similar horizontal mode shapes and periods. Therefore, *Mass model 1* require least amount of computational effort to simulate horizontal motion with great accuracy compared to the *Benchmark model*.

Simplified models in 3D

- The rigid diaphragm model cannot capture any vertical modes because of the requirement of boundary condition constrained in vertical direction. However, all horizontal and torsional natural mode shapes and vibration periods matched with great accuracy to the *benchmark*.

- *Shell model 240* showed very accurate tendencies in all vertical, torsional and horizontal modes compared to the *Benchmark model*. Only small differences in the vertical mode shapes could be identified. *Shell model 240* can with great accuracy simulate horizontal, torsional and vertical motion.

- *Shell model 60* showed that the main vertical deformation shape followed the *Benchmark model*, although it was inaccurate in details. For higher mode, the differences decreased. However, even though *Shell model 60* cannot perfectly capture the first mode shape, *Shell model 60* requires significantly less effort compared to *shell model 240*, and, thus, can be a viable option to model building to simulate the effects of vertical ground motions.

9.3 Recommendation for further studies

- Perform time history analyses in 3D of a suite of ground motions to evaluate the accuracy of both *Shell model 60* and *240*. Furthermore, try to create models with element resolution between the element mesh of *Shell model 60* and *240*. Identify the model which requires least amount of computational effort to simulate horizontal and vertical ground motion with reliable accuracy compared to the *Benchmark model*.

- Create the Benchmark model in 2D with a consistent mass approach and compare *Mass model 3* to this new benchmark. Perform time history analysis and eigenvalue to evaluate differences and similarities.

- Model the slab with a suite of different beam elements, and investigate the the accuracy of these compared to an *exact* model with shell or brick elements.
- Provide inelastic analysis for the recommended simplified models

References

[1] Ariaratnam, S. T., and Leung, K. C. K. (1990). "Parametric effect of vertical ground acceleration on the earthquake response of elastic structures." *Can. J. Civ. Engrg.,* Ottawa, **17**(2), 209–217.

[2] Iyengar, R. N., and Shinozuka, M. (1972). "Effect of self-weight and vertical acceleration on the behavior of tall structures during earthquake." *Earthquake Enrgr. and struct. Dyn.*, **1**(1), 69–78.

[3] Gupta, R. K., and Hutchinson, G. L. (1994). "Horizontal and vertical seismic response of torsionally coupled buildings." *Engrg. struct.*, **16**(1), 11–24.

[4] Sadeghvaziri, M. A., and Foutch, D. A. (1991). "Dynamic behavior of RC highway bridges under the combined effect of vertical and horizontal earthquake motions." *Earthquake Engrg. and struct. Dyn.*, **20**(6), 535–549.

[5] Ju, S. H., Liu, C. W., and Wu, K. Z., (2000). "3D Analyses of buildings under vertical component of earthquakes." *Journal of struct. Engrg.*, **126**(10), 1196–1202.

[6] Anil K. Chopra, 2007. *Dynamics Of Structures: Theory and Applications to Earthquake Engineering,* Pearson Education, Upper Saddle River, New Jersey, Third edition.

[7] Robert D. Cook, David S. Malkus, Michael E. Plesha, and Robert J. Witt, 2002. *Concepts and applications of finite element analysis,* John Wiley & Sons, Inc., Fourth edition.

[8] Wang, C.M., Lim, G.T., Reddy, J.N., and Lee, K.H. (2000). "Relationships between bending solutions of Reissner and Mindling plate theories." *Engineering Structrues.*, **23**(2001) 838–849

[9] S. Timoshenko, J. N. Goodier, 1951. *Theory of elasticity*, McGraw-Hill, Inc., Second edition.

[10] Newmark, N. M., 1959. "A Method of Computation for Structural Dynamic." *Journal of the Engineering Mechanics Division* **85**(7): 67–94.

[11] Wang, C.M., Reddy, J.N., and Lee, K.H. (2000). Shear deformable beams and plates: Relationships with Classical Solutions. ELSEVIER, Oxford, UK., First edition.

[12] Hilberg, H. M., and Hughes, T. J. R., (1987). "An Error Analysis of Truncated Starting Condition on Step-by-Step Time Integration: Consequences of Structural Dnymaics." *Earthquake Engineering and Strucural Dynamics*, **15**(7): 901-910.

[13] Newmark, N. M., and Hall, W. J., 1982. *Earthquake spectra and Design,* Earthquake Engineer institute, Berkley, Calif.

[14] Edwars, C. H., and Penney, E. D., 2005. *Differential equations & linear algebra*, Pearson Education International, Upper Saddle River, New Jersey, second edition.

[15] Lowrie, W., 2007. *Fundamental of geophysics.* Cambridge University Press, Second edition.

[16] Calvetti, D., Reichel, L., and Yang, C., 1998: "An implicity restarted Lanczos Method for Large Symmetric Eigenvalue Problems", ETNA.

[17] Dehn, E., 1930. *Algebraic Equations: An introduction of the Theories of Lagrange and Galeois.* Columbia University press.

[18] ANSYS: Release 11.0 Documentation for ANSYS Workbench tutorial.

[19] Digital World tectonic activity map. Online, 8.may 2011.
http://denali.gsfc.nasa.gov/dtam/seismic/

[20] Bergan, P. G., and Syvertsen. G., 1989. *Knekking av søyler og rammer.* Tapir, second edition.

[21] Kant, T., Kumar, S., amd Singh, U. P., 1994. "Shell dynamics with three-dimensional degenrate finite elements." *Department of Civil Engineering,* Indian instituite of technology, Powai, Bombay. **1**(50): 135-146.

[22] Lyly, M., Stenberg, R., Vihinen, T. 1993 "A stabil bilinear element for the reissner-mindlin plate model." *Comput methods Appl. Mech. Engrg* 100: 343-357.

[23] Element properties in OpenSEES, v.2.2.2.f.
Online: http://opensees.berkeley.edu/OpenSees/manuals/usermanual/

[24] Clough, W. R., and Penzien, J., 1993. *Dynamics of structures.* McGraw-Hill, inc, second edition.

[25] Bai, Z., Demmel, J., Dongarra, J., Ruhe, A., and Van der Vorst, H., 2000 *Templates for the Solution of Algebraic Eigenvalue Problems: A practical Guide.* SIAM, Philadelphia.

[26] Press, F., and Siever, R., 1991. *Understanding Earth,* Second edition.

[27] USGS, Sience for changing world. Online
http://earthquake.usgs.gov/learn/faq/?categoryID=2&faqID=26